



HOKKAIDO UNIVERSITY

Title	Carbon Dioxide Ice Glaciers at the South Pole of Mars
Author(s)	Smith, I. B.; Schlegel, N. -j.; Larour, E. et al.
Citation	Journal of Geophysical Research Planets, 127(4), e2022JE007193 https://doi.org/10.1029/2022JE007193
Issue Date	2022-04-26
Doc URL	https://hdl.handle.net/2115/87034
Rights	Copyright 2022 American Geophysical Union.
Type	journal article
File Information	Smith_etal_2022_JGRE_MS-and-Suppl.pdf



Carbon Dioxide Ice Glaciers at the South Pole of Mars

I. B. Smith^{1,2}, N-J. Schlegel³, E. Larour³, I. Isola¹, P. Buhler², N. E. Putzig², R. Greve^{4,5}

¹York University, Toronto, Ontario, Canada M3J 1P3

²Planetary Science Institute, Lakewood, Colorado, 80401

³Jet Propulsion Laboratory, California Institute of Technology, Pasadena, California, 91109

⁴Institute of Low Temperature Science, Hokkaido University, Sapporo 060-0819, Japan

⁵Arctic Research Center, Hokkaido University, Sapporo 001-0021, Japan

Corresponding author: Isaac B Smith (ibsmith@yorku.ca)

Key Points:

- **Carbon dioxide ice has been mapped and modeled at the south pole of Mars**
- **Deposition models cannot explain the volumetric distribution of CO₂ ice, thickness, or distribution**
- **We present geomorphic and modeling evidence that the CO₂ deposits flow as glaciers into basins to reach their observed volumetric distribution**

Abstract:

Massive, kilometer thick deposits of carbon dioxide (CO₂) ice have been detected at the south polar cap of Mars by radar investigations. These deposits are divided into several units that are separated by thin water ice bounding layers. Recent studies investigated the accumulation history of CO₂ ice and found that the deposits most likely formed during several episodes in the past, when Martian obliquity was much lower than now. Those studies, while able to predict total volumes of CO₂ ice consistent with those observed, did not attempt to explain the anomalous three-dimensional distribution (thickness or extent) of CO₂ ice or the ice's offset from the topographic high of the polar cap. In this paper we use a combination of feature analysis and numerical modeling to demonstrate that the CO₂ deposits flow as glaciers and that glacial flow distributes the ice into its current position. Further, this distribution allows the ice to survive during high obliquity excursions.

Plain Language Summary

Carbon dioxide (CO₂) ice is found in a stack of deposits at Mars' south pole. These deposits are situated in basins, where they reach more than one kilometer thick. Previous work suggested that the CO₂ ice should be deposited when the axial tilt of the planet was lower, making the poles colder than they are now; however, the thickness and distribution of this ice should be much thinner than observed if only atmospheric effects are working on the ice. Therefore, the CO₂ ice deposit distribution cannot be explained by atmospheric deposition alone. In this paper, we use glacial modeling and feature analysis to demonstrate that glacial flow better explains the distribution of ice in its present state. In addition, we show that the slopes on the south polar cap act to focus glacial flow into the basins, where it can survive warm periods by sublimating only the uppermost sections when the tilt of the planet is larger than present day.

1. Introduction

Carbon dioxide ice is observed on Mars in various locations and timescales, from ephemeral clouds, to diurnal frost and seasonal caps (Calvin and Titus, 2008), to the south polar residual cap (SPRC, Figure 1) (Kieffer, 1979; Byrne, 2009) and massive CO₂ ice deposits (MCID, Phillips et al., 2011). Most of these can be seen from Earth when geometry and seasons permit, but the thin, high albedo SPRC that persists over decadal time scales was of primary interest for early Mars observations because it may have implied that the entire south polar layered deposits (SPLD, Figure 1) were composed primarily of carbon dioxide ice. This led to laboratory investigations considering the rheological properties of CO₂ ice and its effect on the SPLD.

These investigations demonstrated that CO₂ ice may flow up to 100x faster than water ice at Martian temperatures (Clark and Mullin, 1976; Durham et al., 1999). Based on those strength measurements, Nye et al. (2000) ruled out the possibility of an SPLD composed entirely of CO₂ ice because it would have insufficient strength to maintain its observed shape over the long time periods implied by the SPLD's surface cratering age (Herkenhoff and Plaut, 2000). That study concluded that the CO₂ ice seen in the SPRC must be thin and cover a more rigid water ice cap, a conclusion later supported by higher resolution observations (Byrne and Ingersoll, 2003) and gravity observations that are sensitive to the entire SPLD thickness (Zuber et al, 2007; Wieczorek, 2008). The possibility of CO₂ glaciers was reconsidered when evidence for moraines near the north polar layered deposits was discovered (Kreslavsky and Head, 2011), but no CO₂ glaciers are present in the north today.

That was the state of knowledge until 2011, when observations by the Shallow Radar (SHARAD) instrument (Seu et al., 2007) on Mars Reconnaissance Orbiter (MRO) detected

massive CO₂ ice deposits (MCID) that reside in deep, elongated, curvilinear basins and are buried beneath a thin layer of dusty water ice and the SPRC (Phillips et al., 2011, Figure 2). Using geophysical arguments and layer geometry, the real part of the dielectric constant of the material was determined to be consistent with that of CO₂ ice, up to 1000 m thick locally but averaging ~400 m thick (Phillips et al., 2011; Bierson et al., 2016; Putzig et al., 2018), two orders of magnitude thicker than the SPRC (Byrne and Ingersoll, 2003; Byrne 2009). The thickness of these deposits varies in relationship to the depth of the basins in which they reside, and several isolated deposits are detached from the main, near-contiguous body of ice (Figure 2). The ice volume, as determined by measurements using a recently generated three dimensional (3D) SHARAD data set (Foss et al., 2017) and extrapolation towards the pole, exceeds 16,500 km³, equivalent to $\sim 2.7 \times 10^{15}$ kg (Putzig et al., 2018; Alwarda and Smith 2021). Using the 1,600 kg/m³ density of CO₂ ice (Piqueux et al., 2003), this mass is approximately equal to the mass of the current atmosphere (Guo et al., 2010).

Based on these detections, modeling efforts have attempted to explain the depositional and climatic history of the MCID (Buhler et al., 2019; Manning et al., 2019). They predicted similar timeframes for the initial deposition, which would have began ~510 kyr in the past, but different mechanisms of deposition and preservation. Buhler et al. (2019) and a follow up study (Buhler and Piqueux, 2021) were able to calculate deposition rates through time for these deposits and a total mass that closely approximates that observed by radar (Putzig et al., 2018). The modeling of Manning et al. (2019) predicted that the bounding layers that separate each CO₂ unit would act as seals to protect the CO₂ ice during warm periods, similar to suggestions by Bierson et al. (2016); however, this came with a stratigraphic section of CO₂ ice that was sandwiched between thin H₂O layers. Alwarda and Smith (2021) compared the two models to

SHARAD observations of the stratigraphy and found evidence to support the model presented in Buhler et al. (2019) but not that of Manning et al. (2019). Neither one-dimensional model treated the three-dimensional distribution of CO₂ ice that is observed, leaving that question open for future work. Work from a decade earlier suggested that the distribution of the SPRC, namely the offset from the geographical pole, the average elevation much lower than the highest elevation on the cap, and the presence between 120° W to 45° E (Figures 1 and 2) are caused by large scale topographic forcing of atmospheric dynamics (Colaprete et al. 2005). Extrapolating backwards in time and assuming a similar mechanism for the MCID and the SPRC, this explanation could explain the general location of the MCID but not the three-dimensional distribution, including the thickness or disconnected nature.

Here, through observations (Sections 2 and 3) and modeling (Sections 4 and 5), we demonstrate for the first time that the distribution of the MCID is caused by glacial flow and that uniform atmospheric deposition is insufficient to explain the observations. In Section 6 we discuss the implications of this finding and answer some previously outstanding questions about the distribution of the ice.

2 Geomorphic Observations

We employ datasets from ongoing and past Mars orbiters to characterize the physical state of the CO₂ deposits. Topography is measured with the 512 pixels per degree south polar dataset from the Mars Orbiter Laser Altimeter (MOLA, Smith et al., 2001) and supplemented with a south polar digital terrain model (DTM) from the High Resolution Stereo Camera (HRSC, Neukum and Jaumann, 2004; Putri et al., 2019). Surface features are identified and interpreted with data from the High-Resolution Imaging Science Experiment (HiRISE, McEwen et al.,

2007) and the Context Imager (CTX, Malin et al., 2007) on MRO. Subsurface geometry is measured with three-dimensional data (Foss et al., 2016; Putzig et al., 2018) from SHARD (Seu et al., 2007).

Using MOLA and orbital imagery, we find that the MCID exhibit variable physical characteristics that can be classified as laterally bound, laterally unbound, or partially bound. The first landform is a ~100 m thick deposit that resides on the highest elevation and latitude of the SPLD plateau. Here, the CO₂ ice resides on a level surface and is unbound at the margins (Red Star #1 in Figure 3). Topographic measurements only cover a portion of this deposit, but where it can be measured, the gross morphology resembles a dome. The second type of morphologic expression, laterally bound deposits, is found in two locations at the lowest elevations within closed basins. The two examples express low relief and are physically disconnected from nearby deposits (Red Stars #2 and #3 in Figure 3). Thirdly, at intermediate latitudes and elevations, several other deposits reside in elongated, curvilinear basins. These deposits are bound on two sides by preexisting curvilinear basins that resemble spiral troughs when seen in 3D radar (Alwarda and Smith 2021), and the surfaces dip in the same direction as the underlying topography (Figure 2; Red Stars #4 and #5 in Figure 3). Further, each unit has convex up profiles, at least for the majority of their length, that point in the dip direction. We also note a concave portion in the highest 30 km of Profile 4. In some cases, the surface slope steepens slightly at the lowermost section (Figure 3, Stars #4 and #5). We informally name two of these partially bound deposits Wolf Glacier and Brooks Glacier.

Other features are unique to the thick CO₂ units as well. Over much of the SPRC there are shallow elongated depressions (minor troughs; Smith et al., 2014) that orient perpendicular to the maximum topographic gradient and parallel to the large-scale, parabolic topographic

contours as mapped by MOLA (Figures 3, S1-S3). They are best seen in late summer as dark curvilinear marks within the high albedo SPRC (Figures S1 and S2), have depths that range from 10 to 100 m, and are hypothesized to be sublimation pits (Phillips et al., 2011) or erosional megadunes (Smith et al., 2014). At the highest elevations, near to the lowest slopes, the minor troughs have very small topographic perturbations (<10 m) and have short wavelengths, whereas the deposits at intermediate elevations and greater surface slopes exhibit much larger topographic depressions up to 100 m deep and tens of km wide (Profile #4 in Figure 3). The lowest elevation deposits that reside in closed basins exhibit no minor troughs.

Additionally, smaller surface features include low-relief ridges that vary from 5 to 20 m in height (Figure 4). Near the margins of Wolf and Brooks Glaciers, we observe low ridges that align parallel to the large-scale topographic contours (Figure 4). Similar features are also observed on the margins of the two isolated, lower elevation deposits (red arrows in Figure S4). The locations are indicated by yellow stars in Figure 3.

3 Geologic Interpretation

We interpret the physical attributes observed as indicative of current or relict flow of CO₂ glaciers. For the gross morphology, the landforms we observe are end members of viscous flow with different boundary conditions. The filled basins are the result of glaciers flowing downhill into basins where they are confined and will eventually become fully level. The dome-shaped deposit at the highest plateau of the SPLD resembles unconfined flow of CO₂ over a flat base (e.g. Nye 2000). The elongated deposits at intermediate elevations resemble terrestrial outlet or valley glaciers (Figure S5) that have parabolic topographic contours pointing towards the glacier toe (Figures 3a, S1- S3).

For the elongated, valley-filling deposits, the parabolic contours and the convex-up shape (Figure 3) are a result of the fluid responding to gravitational stress. The convex-up shape is indicative of an ablation zone in terrestrial outlet glaciers, whereas the concave-up region, near the head of Wolf Glacier, is more typical of an accumulation zone (Cuffey and Paterson, 2010, Figures 4.4 and 11.7). We don't believe that the glacier is accumulating from atmospheric deposition at present, so accumulation may arrive from further south at the ice sheet margin. Unfortunately, that is right at the latitude where MOLA and SHARAD lose coverage; however, topographic data from a HRSC digital terrain model (Putri et al., 2019) suggests that the topography increases with latitude, potentially supporting this interpretation. Furthermore, for Wolf and Brooks Glaciers, we interpret the increased slopes at the terminus of the deposits as glacial toes that steepen because the base does not slide (Stars #4 and #5 in Figure 3).

We interpret the minor troughs (Figure S1 and S2) to be crevasses that form due to the strong topographic gradients that cause elevated stresses and fracturing. We consider flow direction (as demonstrated by the parabolic contours and our modeling results; see Section 5) and find that the crevasses resemble ogives at outlet glaciers in ablation zones (Figure S5); however we believe that the formation mechanism differs from that of ogives because ogives can only form near icefalls (Cuffey and Paterson, 2010), and that is not possible for the minor troughs. Fracturing occurs as a result of gravitational driving stresses overcoming the strength of a mechanically strong but thin (~8 m thick) water-ice layer that overlies and protects the CO₂ deposits (BL₃ in Buhler et al., 2019 and Alwarda and Smith, 2021). Driving stresses are positively influenced by increased gravitational acceleration, surface slope, ice thickness, and ice density and temperature. Because the stresses point downhill, and the water-ice layer is prone to brittle failure at 150 K, the failures will be parallel to the topographic contours, as observed,

matching crevasse formation on terrestrial valley glaciers (Figures S2 and S5). For more discussion about crevasse growth and alternative interpretations regarding the minor troughs, including winds and preferential deposition, see the supplemental material.

We interpret the low-relief ridges (Figures 4 and S4) to be compressional features near the margin of the glacier. They resemble compression ridges found near McMurdo Station, Antarctica (Figure S6), where faster moving ice abuts slower moving ice. This type of buildup of stress usually happens at the lateral margin of a glacier or at the glacial toe in locations where sliding is not prevalent (Cuffey and Paterson, 2010 Figure 11.7).

In an attempt to detect flowing ice, we compared available HiRISE and CTX images of the CO₂ deposits for the longest baseline possible. Our search for surface translation over the relatively short baseline of Mars Reconnaissance Orbiter's time in orbit (~15 years) has not detected any movement. This is unsurprising, as our modeling (See Section 5) suggests that maximum velocities today are $< 0.2 \text{ m yr}^{-1}$, for a maximum translation of $< 3 \text{ m}$ over the lifetime of MRO. HiRISE has resolution capable of seeing this motion translation, but this is not a conservative estimate of flow, so it is likely slower, and we have not identified any noticeable translation yet.

4 Glacial Modeling Methods

To test the formation history of the MCID and SPRC, we perform three-dimensional glacial modeling using the Ice-sheet and Sea-level System Model (ISSM; Larour et al., 2012). ISSM is a state-of-the-art finite element thermo-mechanical ice flow model, capable of simulating transient flow on a regional or continental scale. The ISSM software is open-source

(<http://issm.jpl.nasa.gov>) and is designed as a flexible and scalable platform for the physical modeling of ice flow and the incorporation of data assimilation techniques via inverse control methods (Morlighem et al., 2009). ISSM has an adaptable, anisotropic mesh that can be highly refined in areas of complex ice flow or steep surface topography, and the software itself can handle simulations with millions of degrees of freedom, relying upon a C++ core for dynamic memory allocation and parallelization through multi-processor distributed computing. Ice flow can be modeled in 2 or 3 dimensions (2D/3D) with a number of momentum balance models including a Shallow-Shelf Approximation and the 3D high-order (HO) Blatter/Pattyn model (Blatter, 1995; Pattyn, 2003), a first-order approximation of the full-Stokes equations that assumes hydrostatic balance. The model incorporates stress-balance and mass-transport modules (Larour et al., 2012) and 3D thermal capabilities, that include advection (heat transferred by moving mass) and thermal diffusivity (Seroussi et al., 2013).

To adapt ISSM for Mars, we incorporate Martian gravity (3.71 m/s^2), reasonable geothermal flux (0.025 W/m^2) (Parro et al., 2017), topography (Smith et al., 2001; Putri et al., 2019), surface temperature (150 K locked at the sublimation temperature of the overlying SPRC), and the basal topography mapped with SHARAD to give thickness (Putzig et al., 2018). MOLA 512 PPD data supplied the surface topography (Smith et al., 2001). In our latest simulations, for regions inside of the MOLA data gap, we use surface topography calculated with data from HRSC (Putri et al., 2019). Earlier simulations were completed before we became aware of this dataset, so we performed various extrapolations to fill the data gaps (Table S1). The high latitude basal geometry cannot be constrained with any dataset, so we extrapolate the base of the CO_2 deposits to have zero thickness at the extent of the boundaries made with geologic

mapping (Phillips et al., 2011) and make assumptions about the thickness of the CO₂ units based on that geologic mapping (Table S1).

We also updated the material properties of the model fluid to match CO₂ ice (Table 1): rheology (Cross et al., 2020), heat capacity, thermal conductivity, and density (Piqueux et al., 2003). In these first-order simulations we did not include the top layer of water ice, the bounding layers (Alwarda and Smith, 2021) or the interpreted crevasses but anticipate their effects for future work (Figure S2). Once included, these bounding layers will likely reduce the modeled flow velocity.

Table 1: Inputs to the model

Geothermal Flux	25 mW/m ² (Parro et al., 2017) or 10 mW/m ²	Thermal Conductivity	0.4 W/m/K (Ross and Kargel, 1998)
Gravity	3.71 m/s ²	Activation Energy	67 kJ/mol (Cross et al., 2020)
Deposition area	variable depending on setup: See Table S1	Heat Capacity	700 J/kg/K
Basal friction coefficient	500 (m/s) ^{-1/2}	Stress exponent	n=8 or n=6

The ISSM model domain for the ice cap is made up of a high resolution, anisotropic mesh of 13,500 finite horizontal elements and seven layers for a total of 94,500 individual elements. Mesh resolution cells range from 3.5 km (near the glacier margins) to 4 km (in the middle of the glaciers and in the no-data zones). The 3D thermal model is initialized with a conduction-only solution, forced by a surface temperature of 150 K and a geothermal heat flux of 25 or 10 mW/m². Based on laboratory experiments of CO₂ ice, thermal conductivity is set to a

value of 0.4 W/m/K, and heat capacity is set to 700 J/kg/K (Ross and Kargel, 1998). We initialize ice rigidity (B) using the resulting 3D temperature field, according to a Nye formulation (Nye, 2000) updated with new experimentally determined constants for CO₂ (Cross et al., 2020), relating temperature to the flow law parameter A, where $B=A^{-1/n}$ and has units of s^{1/8}Pa (since n is set to a value of 8 for CO₂) and the activation energy of 67 kJ/mol. We disallow sliding (setting the friction coefficient to 500 [m/s]^{-1/2}) and set the initial thickness everywhere to 1 m (smallest permitted in the model).

To test sensitivity of the model to a variety of factors, we ran simulations with several variables. One variable we adjusted is a geothermal heat flux of 25 or 10 mW/m² fixed throughout the simulation. This allows us to test for the invert-ability of flow rate to find a constraint on geothermal flux. To test flow rates, we completed simulations in which flow was disabled or the stress exponent was varied (n=8 or n=6). n=6 was chosen to split the difference between two solutions by Durham et al. (1999) with n=5.6 (“recommended rheology”) and n=7 (“plausible best estimate”). We also varied the domain size to test how the initial distribution of accumulation affected the final distribution of ice. See Table S1 for a full list of differences between the model runs.

Our deposition area for Simulation 08-11 is approximately 17:8 larger than that modeled by Buhler et al. (2019), and so we divide the surface mass balance (SMB) by that ratio to match the total CO₂ budget for the planet. We follow this ratio rule for the other simulations in which we varied the domain size. This implicitly assumes that CO₂ is not depositing in large quantities elsewhere, justified because the presently observed albedo and emissivity of the SPRC are significantly higher than other (seasonal) CO₂ deposits on Mars (Paige and Ingersoll, 1985), belying their locations and stability.

In two simulations, we modeled the current topography and ice thickness to estimate the speed of glaciers today. The geothermal flux was set to 10 mW/m^2 and 25 mW/m^2 for simulations 12 and 36, respectively. Unlike the historical simulations, these were only run for 1,000 years to establish model convergence.

Finally, for each setup we solve a full transient solution (forward run) that includes a thermal solution with convection plus advection. The only varying input during any simulation is the SMB from Buhler et al. (2019). The transient solves the mass transport, stress balance, and thermal models through time, resulting in 3D solutions fields for ice thickness, ice velocity, and ice temperature. Inputs to the model are in Tables 1 and S1, and results are discussed in the next section.

5 Glacial Model Results:

During our model runs, CO_2 ice was deposited uniformly over the entire model domain, and we measured the total thickness of the ice in each cell as well as the temperature and three-component velocity. We also tracked the global ice mass and the maximum values of thickness, temperature, and velocity globally.

In order to have a basis for comparison, in Simulation 19, we ran the model with flow turned off and found that the entire model domain accumulated and lost ice uniformly, as expected. Total ice volume and ice volume per horizontal grid cell tracked the SMB, either increasing or decreasing, when SMB was positive or negative. The final result was a uniformly 44 m thick deposit with no lateral variation (see Supplemental Material and Videos). This result did not match the observed distribution of MCID in any way.

For the models with flow turned on, no matter the variable being tested, the ice flowed downhill following the gravitational stresses and topographic gradient. Due to the large stress exponent governing the stress response of CO₂ ice (n=8 compared to n=3 for H₂O ice; Cross et al., 2020), ice that is deposited on steeper slopes experiences much faster flow than on lower slopes, even if it is thinner or warmer. We compared Simulation 20-24 with n=8 to the 'no flow' Simulation 19, which was otherwise identical, and found that the icy distribution was much closer to that observed by Putzig et al. (2018) and Alwarda and Smith (2021).

Stress Exponent:

To test the sensitivity of the model to stress exponent, Simulation 25-26 was run with a stress exponent of n=6 (a possible solution from Durham et al. (1999)) but otherwise identical to Simulations 20-24 and 19. The horizontal velocity near steep slopes dropped by nearly 30% from a max of 0.67 m/s to a max of 0.48 m/s. Likewise, for maximum thickness, the simulation with n=6 had a much lower value of ~360 m compared to the thicker ~560 m for n=8. The total volume at the end of the simulation was 9% lower for the n=6 simulation than for the otherwise equivalent n=8 case. Because the results of the higher stress exponent simulations were a closer match to the observations of Mars, we interpret this to support the laboratory measurements of Cross et al. (2020).

From all of our simulations with flow turned on, we find that the high stress exponent acts to focus the CO₂ ice into pre-existing basins where it reached more than 500 m thickness except in the n=6 case (Figures 5 and 6, Supplemental Videos), leaving many locations with thinner ice. We interpret this process to be analogous to a lake serving as a catchment for rainfall. Rain accumulates only a few cm over a large area, but the level of the lake that catches

this entire volume has a smaller area and will experience a much greater rise (Figure 7.4). Compared to flowing water ice on Earth, the ~63% reduction in gravity on Mars partially offsets the higher density of CO₂ ice (~1600 kg/m³ vs. 980 kg/m³ for water ice), so the stresses per unit thickness are 60% lower than what H₂O glaciers experience on earth. However, the weaker rheology of the CO₂ ice on slopes due to the higher stress exponent more than compensates for the lower gravitational stresses, and flow velocities reach several tens of cm per year for the steepest slopes during times of greatest SMB (Figures 5 and 6, Supplemental Material). Locations with low slopes, including where ice is present today, had much more subdued velocities.

For all simulations with flow turned on, the greatest flow rates are always near steep slopes. Additionally, they always occur during periods of positive SMB, lagging slightly behind periods of maximum positive SMB because accumulation is ongoing (Figure 6). The maximum velocity reached for any point over the entire domain and duration exceeds 0.65 m/year. Velocity may approach 0 m yr⁻¹ for multiple reasons: locally for periods in which the ice is very thin and SMB is negative, and on low slopes.

Domain size:

To test the hypothesis that the area over which the ice is deposited affects the outcome, we ran simulations over four domain sizes and scaled the SMB appropriately. We find that the total ice remaining at the end of the simulation does not change meaningfully; however, the distribution varies strongly. In larger simulations, where greater SPLD area was included, there were more depressions for the MCID to enter and pond. This meant less CO₂ ice accumulated in the basins where we find it today and that ice accumulated where it is not observed, an overall

weaker agreement between observations and modeling for the larger domains. We interpret this to support previous work showing that atmospheric dynamics controls where CO₂ is deposited (Colaprete et al., 2005) and that the SPRC is responsive to where CO₂ ice is deposited and sublimated (Buhler et al., 2019). We therefore we find that the modeling supports an interpretation in which the ice that was deposited over the last 600 kyr was limited in aerial extent to something approximately the size of the current SPRC and that if it had been deposited more widely, we would find ice in more locations.

Geothermal flux:

Since geothermal flux and thermal conductivity are fixed in the model, and the thermal response rate is faster than the accumulation/sublimation rate, subsurface temperatures are governed linearly by deposit thickness (Figure 6). Some simulations were run with a low end member of 10 mW/m² for south polar geothermal flux to be conservative. For other simulations, we changed the geothermal flux to 25 mW/m² to align with the currently accepted range of values (Parro et al., 2017). Changing the geothermal flux permits us to assess the sensitivity of this model to heat input from below.

We compare Simulation 38 to Simulation 08-11 that had identical inputs except for the surface topography and the geothermal flux. For comparison, we sample four locations outside of the data gap, anticipating that their distance from the data gap isolates them somewhat from stresses that cannot be constrained. We also consider the maximum values for velocity, thickness, and temperature; however, these fall within the data gap and are based on incomplete assumptions, so we do not include them in this discussion.

At the four locations that we sampled between Simulations 38 and 08-11 (Figure 5), the basal temperature for the higher geothermal flux increased as expected, by more than 15 K at Site 4. The velocity at Site 1 was the fastest that we sampled and had a modest enhancement of approximately 8% during the majority of the simulation (e.g. from 0.305 m yr^{-1} to $.327 \text{ m yr}^{-1}$). Surprisingly, during the period with high, positive SMB at 470 kya, the lower geothermal flux simulation had a faster velocity (0.633 m yr^{-1} and $.631 \text{ m yr}^{-1}$). Greater velocity enhancements due to increased geothermal flux may be anticipated; however, the fastest ice is always at locations with steep slopes that tend to be thinner than average, not at the thickest locations that have lower overall slopes, where the base would be warmer. This may have affected the surprisingly higher flow rate for the lower geothermal flux at Site 1, with total accumulation (SMB identical, but a "backlog" of ice built up) causing faster flow. The final spatial distribution of the ice also shows modest differences, and the final volume was nearly equivalent.

Comparing the final thickness at Site 4, Simulation 08-11 surprisingly has thicker ice than Simulation 38, 556 m vs. 547 m, respectively. Likewise, Simulation 38 had a slightly smaller total mass than Simulation 08-11 at the end. It's unclear what causes this surprising result, where warmer ice does not fill the basin as full as the cooler ice. One hypothesis that we will test going forward is that there is spatial separation between the fastest ice and the thickest ice. The fastest ice is on steep slopes and is much thinner than the thick (warmest) regions with shallow slopes. Being thinner, they were only weakly affected by the increase in geothermal flux, whereas the basins, where ice is thicker and warmer, had lower/slower slopes. Alternatively, changing the the surface topography in the MOLA data gap from our original interpolation to the published result of Putrie et al., 2019 may have had a measureable effect.

Comparison to Observations:

Using the inputs described above, our model produces deposit thicknesses and distributions that resemble those observed by SHARAD (Figures 2 and 5). There are two exceptions: inside of the data gap at high latitudes and at the rad star in Figures 5 and S8. For the high latitudes, no direct comparison is possible due to the lack of SHARAD data near the poles. At the starred location, the model predicts a hundreds of meters thick unit of MCID ice, but none has been detected by SHARAD analysis (Figures 2, S8). Surface feature mapping has revealed that a relict unit called A0 can be found at this location (Thomas et al., 2009, 2016). A0 is a distinctive unit, older and thicker than all other SPRC units, and A0 exposures elsewhere correspond spatially to detection of the MCID, leaving the possibility that this location has MCID that is too thin to detect with SHARAD. Similar to our domain size findings above, we interpret this result to mean that the domain size of these simulations encompassed too large of an area of deposition on the steep SPLD margin near the star, leaving a deposit there that doesn't match observations.

6 Discussion

Previous work suggested that cycles of CO₂ deposition and sublimation built up the alternating layers of CO₂ and H₂O ice that compose the MCID (Bierson et al., 2016; Buhler et al., 2019; Manning et al., 2019). Bierson et al. (2016) and Manning et al. (2019) proposed that H₂O bounding layers form during periods of CO₂ sublimation, eventually cutting off the sublimation to preserve the MCID, but they did not propose how the bounding layers were

deposited. Bierson et al. (2016) also observed that the CO₂ ice was preferentially thicker in depressions, but did not provide a physical mechanism for this observation. Buhler et al. (2019) showed that sublimation lags form H₂O bounding layers during periods of CO₂ ablation. That study was able to match the thickness ratio of MCID layers at one specific location, but made no attempt to explain the 2D or 3D distribution of the CO₂ ice. Neither model explained why the CO₂ ice concentrated in the valleys, how the final volumetric distribution occurred, or the unit thickness and stratification outside of one location. Alwarda and Smith (2021) found stratigraphic evidence supporting the Buhler model in the sequence of bounding layers but didn't offer any further explanations for the mass distribution.

Our modeling addresses all of these open questions. In particular, our results explain the spatial and volumetric distribution of the MCID that was heretofore unexplained. While depositing, the ice flows downslope into the depressions (Figure 7), creating the thickest deposits that can survive periods of negative SMB. The thinned deposits that lost mass to flowing ice do not survive sublimation periods, leaving the basement material exposed. Based on our Simulation 19, with flow turned off, the total SMB over 600 kyr is positive, but only enough to grow a few tens of meters of ice in total, uniformly over the domain, far short of the 400-1,000 m thickness estimated for the thickest observed deposits, and incompatible with the zero observed thickness in many locations within the accumulation domain. Thus, by focusing the ice into depressions, glacial flow explains the regions with thinner and thicker distributions and the persistence through periods with negative SMB, something a model without flow or highly preferential deposition cannot do. In that vein, if the flow speed is effectively reduced (via lowering the stress exponent or lowering geothermal flux) then less ice ponds to survive the negative SMB periods, and the total volume of ice at the end of the simulation is reduced.

However, we found that changing the geothermal flux has a smaller effect than anticipated, likely because the thicker portions that have warmer basal temperatures are in basins (with shallower slopes), and the thinner, steeper sloped regions don't experience strong temperature increases that would accelerate flow.

Our modeling results demonstrate that glacial flow focused wide-scale accumulation into the curvilinear basins during periods of positive SMB and that the massive ice persists for long durations only in locations where the ice accumulates to thicknesses greater than the amount removed during the subsequent sublimation period with negative SMB (Figure 7.3).

Simulations with a wider accumulation domain result in a worse fit between modeled and observed mass distribution, namely, the resulting MCID is thinner in important regions and more widespread, filling basins that have no CO₂ ice present today. This represents a major divergence that goes away with smaller model domains and supports the hypothesis of Colaprete et al. (2005) who found that atmospheric dynamics created the SPRC general distribution that we see today, a likely indicator of where the MCID deposition occurred over the past 600 kyr. Secondly, this supports the hypothesis from Buhler et al. (2019) that the SPRC and MCID are linked in formation and evolution (and spatially linked) because a wider accumulation of CO₂ ice over the duration of the model would have resulted in finding more MCID deposits than what has been observed, and thus a more widespread SPRC.

7 Conclusion

In this work we have identified numerous geomorphic features that are indicative of glacial flow of CO₂ units at Mars' south pole. The gross morphology and topographic contours

of the CO₂ deposits, plus smaller features of crevasses and compression ridges, resemble the morphology of terrestrial glaciers.

To support the glacial interpretation, we updated the Ice-sheet and Sea-level System Model to work with martian conditions and flowing CO₂ ice using newly updated rheological laws (Cross et al., 2020). Using these setup conditions, along with known topography and unit thickness, we input the surface mass balance from the most recent 600 kyr as modeled by Buhler et al. (2019). We find atmospherically deposited CO₂ ice will flow into existing topographic basins where it will pond. The final distribution generally corresponds in location and thickness to observed deposits (Putzig et al., 2018).

We ran models of varying distributions of ice deposition and ice flow laws and found that 1) simulations with reduced flow rates cannot reproduce the observed distribution of CO₂ ice and that 2) if the ice is deposited over a larger area, then the final result diverges in thickness and distribution from what we observe. The results support those of Buhler et al. (2019) who modeled the surface mass balance over time and of Colaprete et al. (2005) who found evidence that supports a domain of deposition consistent with the current SPRC.

In summary, glacial flow of atmospherically deposited CO₂ ice explains the observed volumetric distribution of the massive CO₂ ice deposits at the south pole of Mars, and glacial flow has been responsible for focusing widespread CO₂ accumulation into the curvilinear basins, where it has persisted for ~510 kyr, even through periods of net loss. Model results suggest that the deposits are flowing presently but at a ~1/3 reduced rate from their high flow periods, when SMB was at its maximum, at $\sim 4.8 \times 10^5$ years before present (Figure 6). Glacial flow thus provides context for the resulting location, thickness, surface properties, and flow rate of the

observed CO₂ deposits along with providing supporting evidence as to the origin and position of the SPRC.

Other exotic glacial landforms have been found in the Solar System, with the detection of an N₂ ice sheet near the equator of Pluto (Stern et al., 2015). This feature appears to have a very young surface age and exhibits evidence for thermally or sublimation driven convection cells (McKinnon et al., 2016; Morison et al., 2021). Other bodies are suspected to have thick, plastic, exotic ice deposits on their surfaces such as the moon Umbriel (Sori et al., 2017). With the increasing evidence for bodies of exotic ice present in the Solar System, there is a greater need to perform laboratory measurements to determine physical constants of exotic ices and to develop glacial models capable of quantitatively testing them. This in turn will test observations and interpretations, and enable us to invert for their climatic histories.

Acknowledgements: We thank David Goldsby for helpful comments and honor the memory of Roger Phillips, who provided excellent insight into this investigation. Portions of this work were supported by NASA grants NH16ZDA001N and NNX17AC62G and a Canada Research Chair.

Data Availability Statement:

3D SHARAD data used in this manuscript are publicly available at <https://doi.org/10.17189/QK73-ZX21>.

MOLA data are available at <https://doi.org/10.17189/1519460>.

HiRISE data are available at <https://doi.org/10.17189/1520179>.

CTX data can be found at <https://doi.org/10.17189/1520266>.

ISSM is publically available at <https://issm.jpl.nasa.gov/>.

ISSM Mars outputs used in this manuscript can be found in Smith (2022a, 2022b, 2022c)

References:

- Alwarda, R., Smith, I.B., 2021. Stratigraphy and Volumes of the Units Within the Massive Carbon Dioxide Ice Deposits of Mars. *J. Geophys. Res. Planets* 126, e2020JE006767. <https://doi.org/10.1029/2020JE006767>
- Bierson, C.J., Phillips, R.J., Smith, I.B., Wood, S.E., Putzig, N.E., Nunes, D., Byrne, S., 2016. Stratigraphy and evolution of the buried CO₂ deposit in the Martian south polar cap. *Geophys. Res. Lett.* 43, 4172–4179. <https://doi.org/10.1002/2016GL068457>
- Buhler, P.B., Ingersoll, A.P., Piqueux, S., Ehlmann, B.L., Hayne, P.O., 2019. Coevolution of Mars's atmosphere and massive south polar CO₂ ice deposit. *Nat. Astron.* 1–8. <https://doi.org/10.1038/s41550-019-0976-8>
- Buhler, P.B., Piqueux, S., 2021. Obliquity-Driven CO₂ Exchange Between Mars' Atmosphere, Regolith, and Polar Cap. *J. Geophys. Res. Planets* 126, e2020JE006759. <https://doi.org/10.1029/2020JE006759>
- Byrne, S., 2009. The polar deposits of Mars. *Annu. Rev. Earth Planet. Sci.* 37, 535–560.
- Byrne, S., Ingersoll, A.P., 2003. A Sublimation Model for Martian South Polar Ice Features. *Science* 299, 1051–1053. <https://doi.org/10.1126/science.1080148>
- Calvin, W.M., Titus, T.N., 2008. Summer season variability of the north residual cap of Mars as observed by the Mars Global Surveyor Thermal Emission Spectrometer (MGS-TES). *Planet. Space Sci.* 56, 212–226. <https://doi.org/10.1016/j.pss.2007.08.005>
- Clark, B.R., Mullin, R.P., 1976. Martian glaciation and the flow of solid CO₂. *Icarus* 27, 215–228. [https://doi.org/10.1016/0019-1035\(76\)90005-1](https://doi.org/10.1016/0019-1035(76)90005-1)
- Colaprete, A., Barnes, J.R., Haberle, R.M., Hollingsworth, J.L., Kieffer, H.H., Titus, T.N., 2005. Albedo of the south pole on Mars determined by topographic forcing of atmosphere dynamics. *Nature* 435, 184–188.
- Cross, A.J., Goldsby, D.L., Hager, T.F., Smith, I.B., 2020. The Rheological Behavior of CO₂ Ice: Application to Glacial Flow on Mars. *Geophys. Res. Lett.* 47, e2020GL090431. <https://doi.org/10.1029/2020GL090431>
- Cuffey, K.M., Paterson, W.S.B., 2010. *The Physics of Glaciers*. Academic Press.
- Durham, W.B., Kirby, S.H., Stern, L.A., 1999. Steady-state flow of solid CO₂: Preliminary results. *Geophys. Res. Lett.* 26, 3493–3496. <https://doi.org/10.1029/1999GL008373>
- Foss, F., Putzig, N., Campbell, B., Phillips, R., 2017. 3D imaging of Mars' polar ice caps using orbital radar data. *Lead. Edge* 36, 43–57. <https://doi.org/10.1190/tle36010043.1>
- Guo, X., Richardson, M.I., Soto, A., Toigo, A., 2010. On the mystery of the perennial carbon dioxide cap at the south pole of Mars. *J. Geophys. Res. Planets* 115, E04005. <https://doi.org/10.1029/2009JE003382>
- Herkenhoff, K., Plaut, J.G., 2000. Surface Ages and Resurfacing Rates of the Polar Layered Deposits on Mars. *Icarus* 144, 243–253. <https://doi.org/10.1006/icar.1999.6287>
- Kieffer, H.H., 1979. Mars south polar spring and summer temperatures: A residual CO₂ frost. *J. Geophys. Res. Solid Earth* 84, 8263–8288. <https://doi.org/10.1029/JB084iB14p08263>
- Kreslavsky, M.A., Head, J.W., 2011. Carbon dioxide glaciers on Mars: Products of recent low obliquity epochs (?). *Icarus* 216, 111–115. <https://doi.org/10.1016/j.icarus.2011.08.020>
- Malin, M.C., Bell, J.F., Cantor, B.A., Caplinger, M.A., Calvin, W.M., Clancy, R.T., Edgett, K.S., Edwards, L., Haberle, R.M., James, P.B., Lee, S.W., Ravine, M.A., Thomas, P.C., Wolff, M.J., 2007. Context Camera Investigation on board the Mars Reconnaissance Orbiter. *J. Geophys. Res. Planets* 112, n/a-n/a. <https://doi.org/10.1029/2006JE002808>

- Manning, C.V., Bierson, C., Putzig, N.E., McKay, C.P., 2019. The formation and stability of buried polar CO₂ deposits on Mars. *Icarus* 317, 509–517. <https://doi.org/10.1016/j.icarus.2018.07.021>
- McEwen, A.S., Eliason, E.M., Bergstrom, J.W., Bridges, N.T., Hansen, C.J., Delamere, W.A., Grant, J.A., Gulick, V.C., Herkenhoff, K.E., Keszthelyi, L., 2007. Mars reconnaissance orbiter's high resolution imaging science experiment (HiRISE). *J. Geophys. Res. Planets* 1991–2012 112.
- McKinnon, W.B., Nimmo, F., Wong, T., Schenk, P.M., White, O.L., Roberts, J.H., Moore, J.M., Spencer, J.R., Howard, A.D., Umurhan, O.M., Stern, S.A., Weaver, H.A., Olkin, C.B., Young, L.A., Smith, K.E., the New Horizons Geology, Team, G. and I.T., 2016. Convection in a volatile nitrogen-ice-rich layer drives Pluto's geological vigour. *Nature* 534, 82–85. <https://doi.org/10.1038/nature18289>
- Morison, A., Labrosse, S., Choblet, G., 2021. Sublimation-driven convection in Sputnik Planitia on Pluto. *Nature* 600, 419–423. <https://doi.org/10.1038/s41586-021-04095-w>
- Neukum, G., Jaumann, R., 2004. HRSC: the High Resolution Stereo Camera of Mars Express. Presented at the Mars Express: the Scientific Payload, pp. 17–35.
- Nye, J.F., Durham, W.B., Schenk, P.M., Moore, J.M., 2000. The Instability of a South Polar Cap on Mars Composed of Carbon Dioxide. *Icarus* 144, 449–455. <https://doi.org/10.1006/icar.1999.6306>
- Parro, L.M., Jiménez-Díaz, A., Mansilla, F., Ruiz, J., 2017. Present-day heat flow model of Mars. *Sci Rep* 7, 45629. <https://doi.org/10.1038/srep45629>
- Phillips, R.J., Davis, B.J., Tanaka, K.L., Byrne, S., Mellon, M.T., Putzig, N.E., Haberle, R.M., Kahre, M.A., Campbell, B.A., Carter, L.M., Smith, I.B., Holt, J.W., Smrekar, S.E., Nunes, D.C., Plaut, J.J., Egan, A.F., Titus, T.N., Seu, R., 2011. Massive CO₂ Ice Deposits Sequestered in the South Polar Layered Deposits of Mars. *Science* 332, 838–841. <https://doi.org/10.1126/science.1203091>
- Piqueux, S., Byrne, S., Richardson, M.I., 2003. Sublimation of Mars's southern seasonal CO₂ ice cap and the formation of spiders. *J. Geophys. Res. Planets* 108, 5084. <https://doi.org/10.1029/2002JE002007>
- Putri, A.R.D., Sidiropoulos, P., Muller, J.-P., Walter, S.H.G., Michael, G.G., 2019. A New South Polar Digital Terrain Model of Mars from the High-Resolution Stereo Camera (HRSC) onboard the ESA Mars Express. *Planet. Space Sci.* 174, 43–55. <https://doi.org/10.1016/j.pss.2019.02.010>
- Putzig, N.E., Smith, I.B., Perry, M.R., Foss, F.J., Campbell, B.A., Phillips, R.J., Seu, R., 2018. Three-dimensional radar imaging of structures and craters in the Martian polar caps. *Icarus, Mars Polar Science VI* 308, 138–147. <https://doi.org/10.1016/j.icarus.2017.09.023>
- Seelos, K.D., Brown, A.J., Calvin, W.M., Titus, T.N., Smith, I.B., Murchie, S.L., 2016. Exploring Mars' South Polar Residual Cap Units Using CRISM Data: Search for the Signature of Buried Ice Layers. Presented at the Lunar and Planetary Science Conference, p. 2130.
- Seu, R., Phillips, R.J., Biccari, D., Orosei, R., Masdea, A., Picardi, G., Safaeinili, A., Campbell, B.A., Plaut, J.J., Marinangeli, L., 2007. SHARAD sounding radar on the Mars Reconnaissance Orbiter. *J. Geophys. Res.* 112, E05S05.
- Smith, D.E., Zuber, M.T., Frey, H.V., Garvin, J.B., Head, J.W., Muhleman, D.O., Pettengill, G.H., Phillips, R.J., Solomon, S.C., Zwally, H.J., 2001. Mars Orbiter Laser Altimeter:

- Experiment summary after the first year of global mapping of Mars. *J. Geophys. Res.-Planets* 106.
- Smith, Isaac. (2022). Mars ISSM simulation output (Version 1) [Data set]. Zenodo. <https://doi.org/10.5281/zenodo.6366163>
- Smith, Isaac. (2022). Mars ISSM simulations model files 1 [Data set]. Zenodo. <https://doi.org/10.5281/zenodo.6384723>
- Smith, Isaac. (2022). Mars ISSM simulations model files 2 [Data set]. Zenodo. <https://doi.org/10.5281/zenodo.6384732>
- Smith, I.B., Holt, J.W., Spiga, A., Howard, A.D., Parker, G., 2013. The spiral troughs of Mars as cyclic steps. *J. Geophys. Res. Planets*. <https://doi.org/10.1002/jgre.20142>
- Smith, I.B., Spiga, A., Holt, J.W., 2015. Aeolian processes as drivers of landform evolution at the South Pole of Mars. *Geomorphology, Planetary Geomorphology: Proceedings of the 45th Annual Binghamton Geomorphology Symposium, held 12-14 September 2014 in Knoxville, Tennessee, USA* 240, 54–69. <https://doi.org/10.1016/j.geomorph.2014.08.026>
- Sori, M.M., Bapst, J., Bramson, A.M., Byrne, S., Landis, M.E., 2017. A Wunda-full world? Carbon dioxide ice deposits on Umbriel and other Uranian moons. *Icarus* 290, 1–13. <https://doi.org/10.1016/j.icarus.2017.02.029>
- Stern, S.A., Bagenal, F., Ennico, K., Gladstone, G.R., Grundy, W.M., McKinnon, W.B., Moore, J.M., Olkin, C.B., Spencer, J.R., Weaver, H.A., Young, L.A., Andert, T., Andrews, J., Banks, M., Bauer, B., Bauman, J., Barnouin, O.S., Bedini, P., Beisser, K., Beyer, R.A., Bhaskaran, S., Binzel, R.P., Birath, E., Bird, M., Bogan, D.J., Bowman, A., Bray, V.J., Brozovic, M., Bryan, C., Buckley, M.R., Buie, M.W., Buratti, B.J., Bushman, S.S., Calloway, A., Carcich, B., Cheng, A.F., Conard, S., Conrad, C.A., Cook, J.C., Cruikshank, D.P., Custodio, O.S., Ore, C.M.D., Deboy, C., Dischner, Z.J.B., Dumont, P., Earle, A.M., Elliott, H.A., Ercol, J., Ernst, C.M., Finley, T., Flanigan, S.H., Fountain, G., Freeze, M.J., Greathouse, T., Green, J.L., Guo, Y., Hahn, M., Hamilton, D.P., Hamilton, S.A., Hanley, J., Harch, A., Hart, H.M., Hersman, C.B., Hill, A., Hill, M.E., Hinson, D.P., Holdridge, M.E., Horanyi, M., Howard, A.D., Howett, C.J.A., Jackman, C., Jacobson, R.A., Jennings, D.E., Kammer, J.A., Kang, H.K., Kaufmann, D.E., Kollmann, P., Krimigis, S.M., Kusnierkiewicz, D., Lauer, T.R., Lee, J.E., Lindstrom, K.L., Linscott, I.R., Lisse, C.M., Lunsford, A.W., Mallder, V.A., Martin, N., McComas, D.J., McNutt, R.L., Mehoke, D., Mehoke, T., Melin, E.D., Mutchler, M., Nelson, D., Nimmo, F., Nunez, J.I., Ocampo, A., Owen, W.M., Paetzold, M., Page, B., Parker, A.H., Parker, J.W., Pelletier, F., Peterson, J., Pinkine, N., Piquette, M., Porter, S.B., Protopapa, S., Redfern, J., Reitsema, H.J., Reuter, D.C., Roberts, J.H., Robbins, S.J., Rogers, G., Rose, D., Runyon, K., Retherford, K.D., Ryschkewitsch, M.G., Schenk, P., Schindhelm, E., Sepan, B., Showalter, M.R., Singer, K.N., Soluri, M., Stanbridge, D., Steffl, A.J., Strobel, D.F., Stryk, T., Summers, M.E., Szalay, J.R., Tapley, M., Taylor, A., Taylor, H., Throop, H.B., Tsang, C.C.C., Tyler, G.L., Umurhan, O.M., Verbiscer, A.J., Versteeg, M.H., Vincent, M., Webbert, R., Weidner, S., Weigle, G.E., White, O.L., Whittenburg, K., Williams, B.G., Williams, K., Williams, S., Woods, W.W., Zangari, A.M., Zirnstein, E., 2015. The Pluto system: Initial results from its exploration by New Horizons. *Science* 350, aad1815. <https://doi.org/10.1126/science.aad1815>

- Thomas, P.C., Calvin, W., Cantor, B., Haberle, R., James, P.B., Lee, S.W., 2016. Mass balance of Mars' residual south polar cap from CTX images and other data. *Icarus* 268, 118–130. <https://doi.org/10.1016/j.icarus.2015.12.038>
- Thomas, P.C., James, P.B., Calvin, W.M., Haberle, R., Malin, M.C., 2009. Residual south polar cap of Mars: Stratigraphy, history, and implications of recent changes. *Icarus* 203, 352–375. <https://doi.org/10.1016/j.icarus.2009.05.014>
- Wieczorek, M.A., 2008. Constraints on the composition of the martian south polar cap from gravity and topography. *Icarus, Mars Polar Science IV* 196, 506–517. <https://doi.org/10.1016/j.icarus.2007.10.026>
- Zuber, M.T., Phillips, R.J., Andrews-Hanna, J.C., Asmar, S.W., Konopliv, A.S., Lemoine, F.G., Plaut, J.J., Smith, D.E., Smrekar, S.E., 2007. Density of Mars' South Polar Layered Deposits. *Science* 317, 1718–1719. <https://doi.org/10.1126/science.1146995>

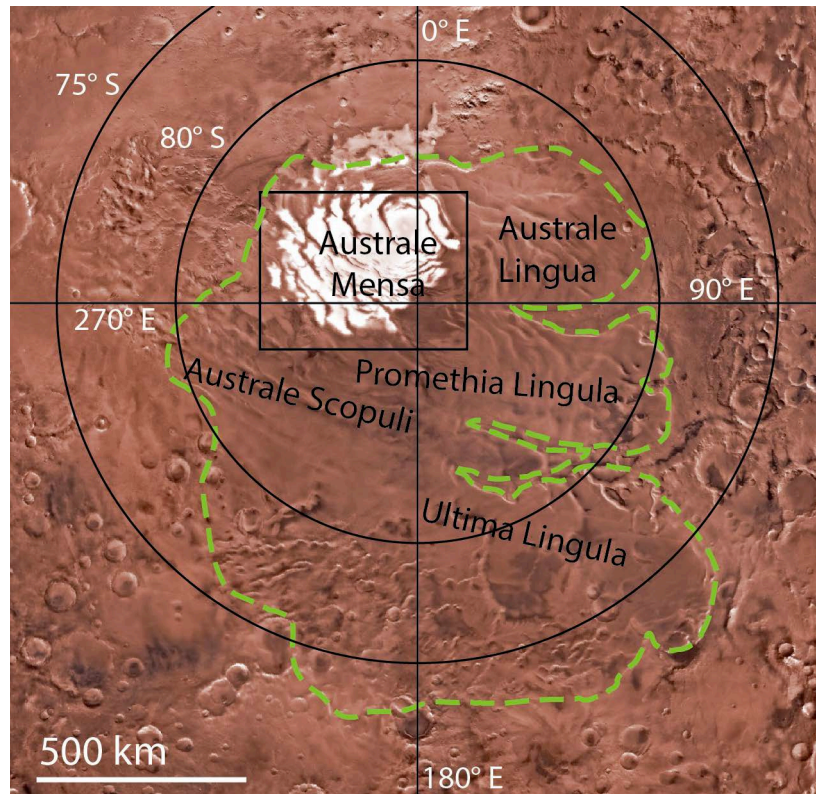


Figure 1: A Viking color mosaic of the South Polar Layered Deposits (SPLD). The South Polar Residual Cap (SPRC) is composed of bright white CO₂ ice. The rest of the ice cap (outlined in green dashed line (Smith et al., 2014) is covered by red dust in spring and summer. Large chasmae, spiral troughs, and scallops are visible. Black box outlines Figure 2a.

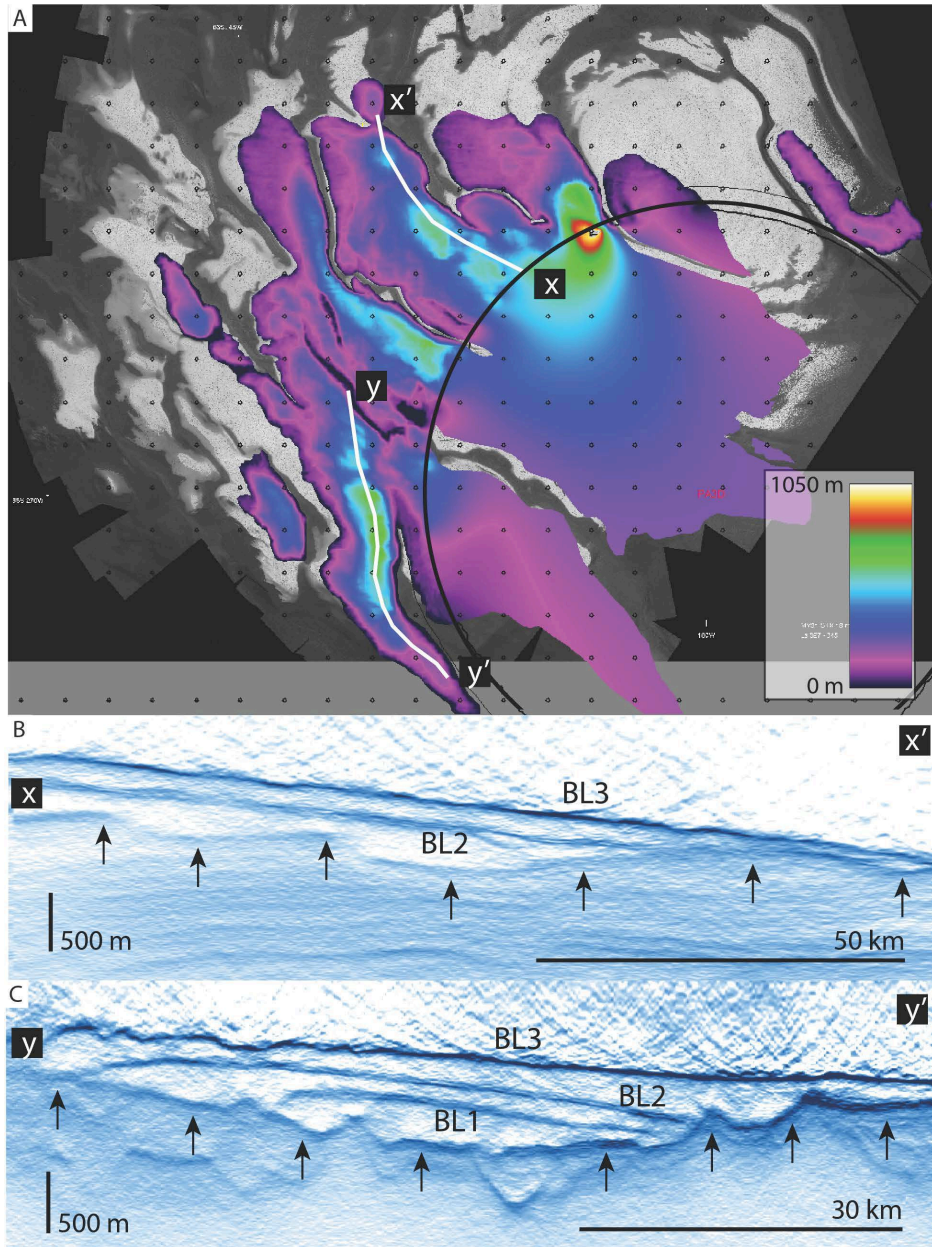


Figure 2: Map of thickness of the CO₂ units over a Context Imager summer mosaic (Thomas et al., 2009) and radar profiles from the recently developed 3D radar data volume (Foss et al., 2017; Putzig et al., 2018). A) Mapped CO₂ ice thickness up to the southern latitude limit of Mars Reconnaissance Orbiter (black circle). Thicknesses inside of the black circle are extrapolated. B) and C) Two radar profiles from the 3D dataset depth converted for $\epsilon'=3.15$, consistent with water ice (the material below the CO₂ units). Black arrows indicate the basal reflection of the CO₂ ice. Bounding Layers (BL) are made of water ice and separate the individual CO₂ units due to past climatic changes (Alwarda and Smith 2021). Surface topography matches that expected for flowing glaciers in bounded, unbounded, and partially bounded geometries (Figure 3).

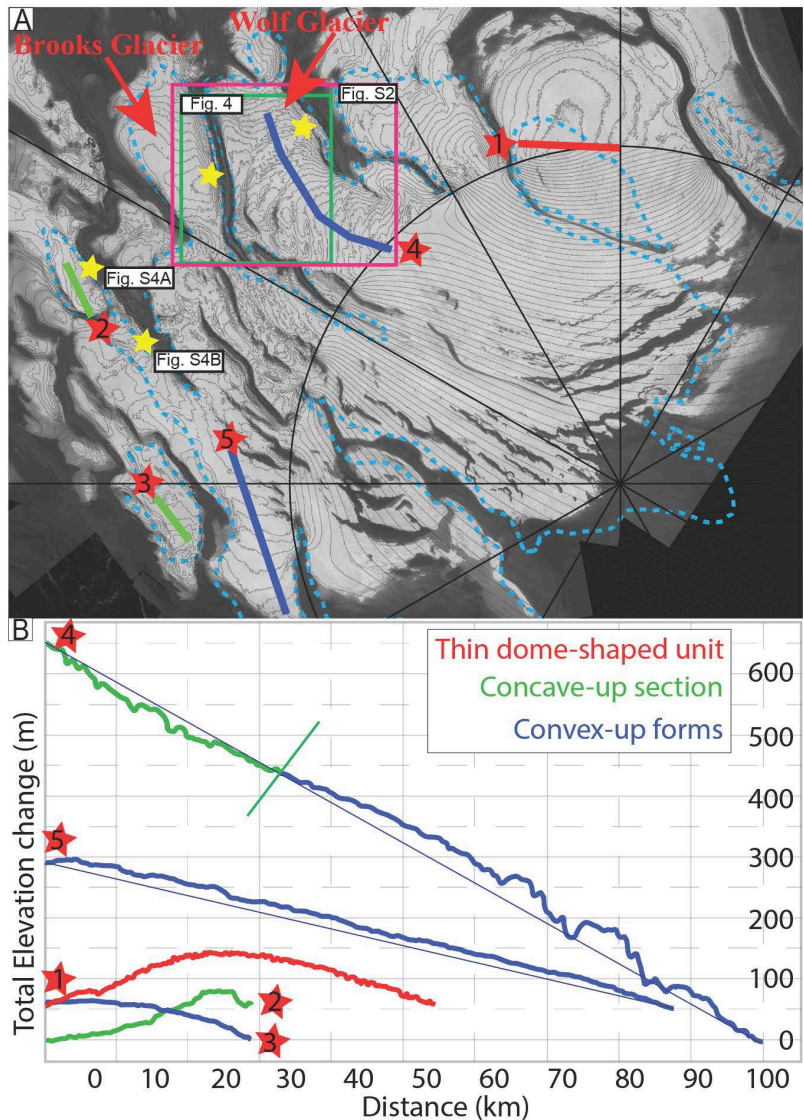


Figure 3: Context map for figures and topographic profiles A) Context Imager (CTX) mosaic (Thomas et al., 2009) with overlain annotation and contour lines. Contour lines are every 25 m of elevation based on MOLA observations (Smith et al., 2001), and indicate arcuate landforms, domes, and flat topography associated with CO₂ deposits. The extent of other figures is shown. Red stars and colorful profiles correspond to (B), yellow stars indicate locations for low relief ridges in Figures 4 and S4. Blue-dashed line is the extent of the MCID. No MOLA or SHARAD data is available inside the black circle. B) Five topographic profiles from (A) demonstrating surface shape of the CO₂ deposits. Profile 1 has a dome shape, to be expected if a viscous fluid were left to relax over a horizontal surface or plateau (Nye et al., 2000). Profiles 2 and 3 are in confined basins that outlie the main ice body. Profiles 3 and 5 are convex-up topographic profiles that resemble those of valley glaciers in terrestrial and Martian settings. Profiles 2 and 4 have concave-up sections that may indicate accumulation zones near the highest elevations (Cuffey and Patterson, 2013). Profile 4 also has deep topographic troughs that correspond to the minor troughs we interpret to be crevasses (see Supplemental Information).

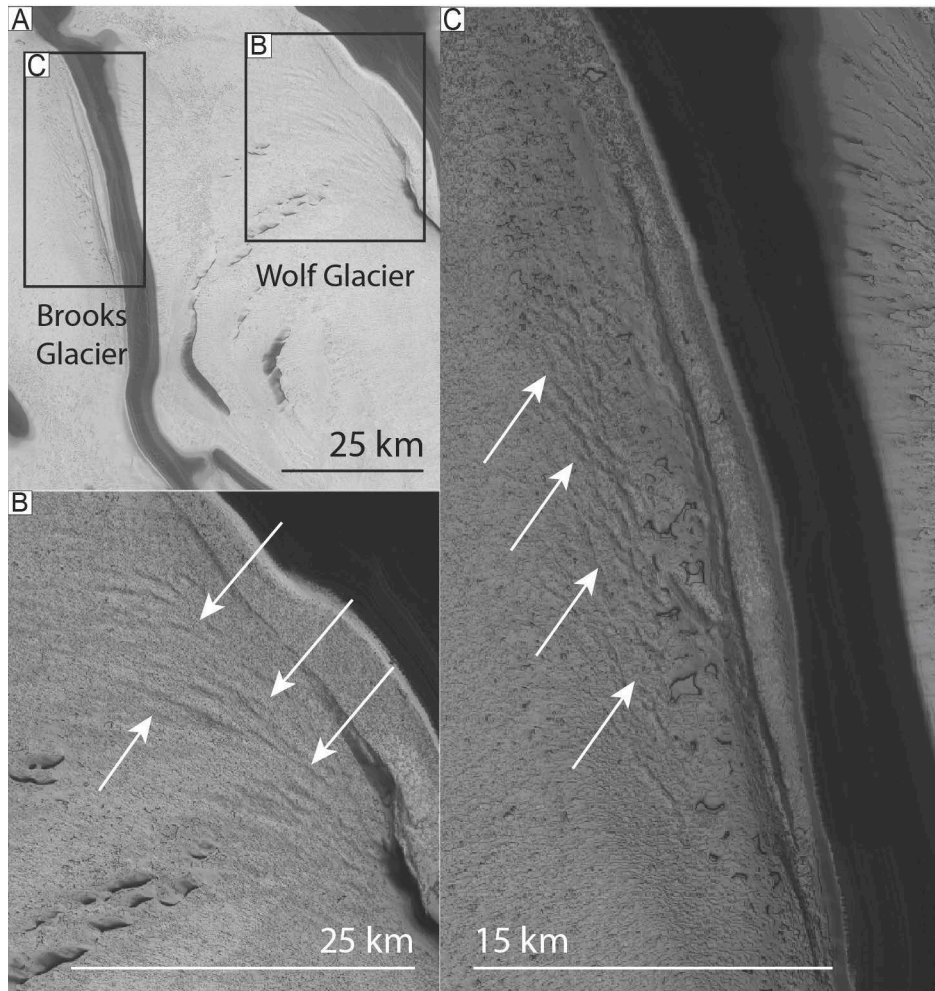


Figure 4: Imagery demonstrating primary and secondary features associated with the CO₂ deposits. A) Summer CTX mosaic of Wolf Glacier exhibiting dark, minor sublimation troughs. The minor troughs align with the gross contours (Figure 2), suggestive of fracturing along the largest stress gradient. B) Low relief ridges at the margin of Brooks Glaciers that reach up to 20 m in amplitude. C) Low relief ridges near the toe and margin of Wolf Glacier are several to 5 m in amplitude. Similar ridges are found in other locations at the south pole of Mars (Figure S4) and on Earth (Figure S6).

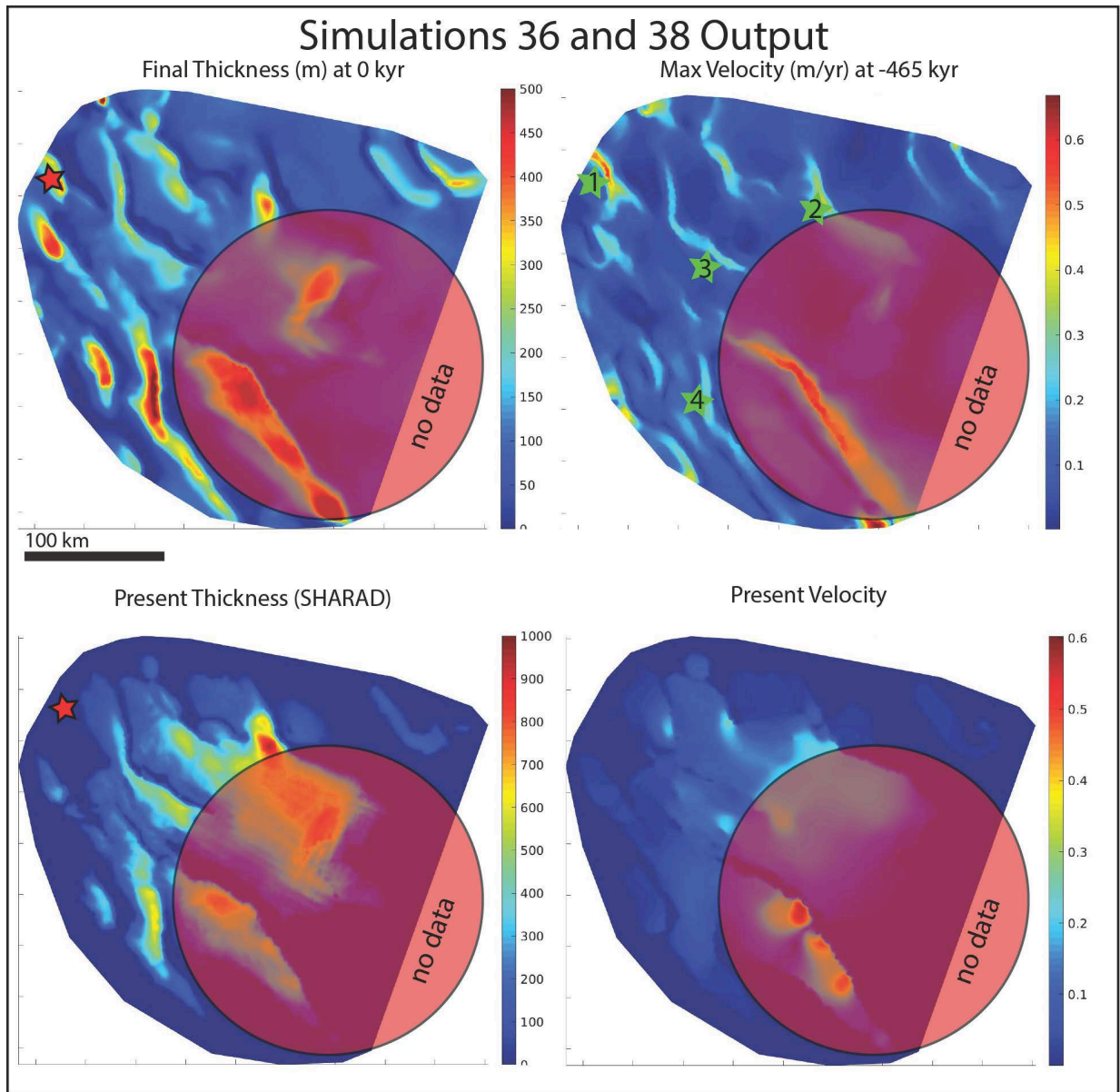


Figure 5: Plots of modeled thickness and velocity above actual thickness and modeled present day velocity. Top Left: Final thickness of Simulation 38. Top Right: Maximum velocity of the simulation (Figure 6) at -470 kyr before present. Bottom Left: Actual thickness using SHARAD measurements (Putzig et al., 2018). Inside of the data hole we use the surface from Putrie et al. (2019) and an interpolation for the base (See supplemental information). Bottom Right: Modeled velocity using actual geometry from Bottom Left Panel. Regions with no radar sounder data to provide thickness are marked by the red circle. Note the different color scale for the two thicknesses. This is to demonstrate the spatial closeness of the final distribution, even if the final thicknesses are different. For this figure with the same scale see Figure S8), Red star indicated the one location outside of the data hole where the modeled thickness strongly diverges from predictions (see Figure S9).

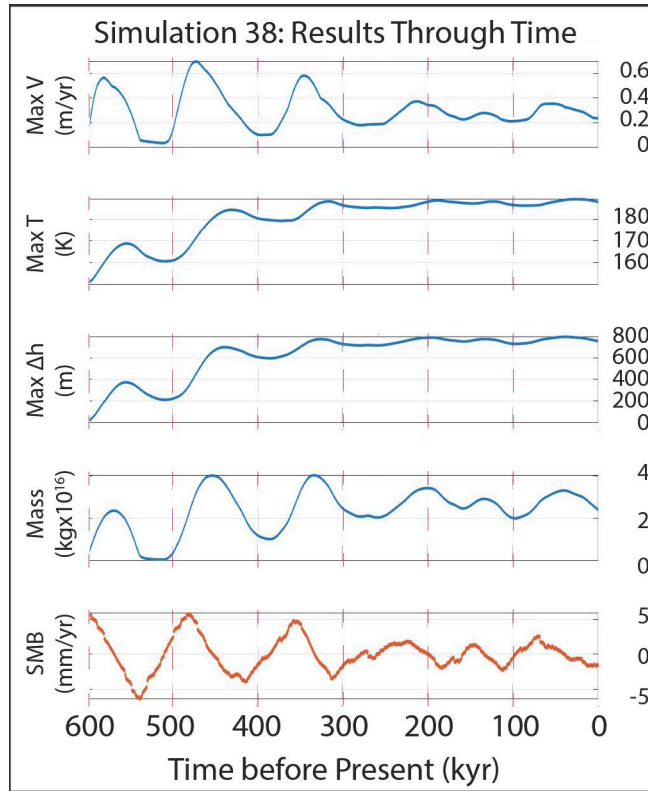


Figure 6: Time series of ISSM Results for Simulation 38. Starting at 600 kyr before present, the model incorporated all Martian conditions (see Section 4). Only the surface mass balance (SMB), provided by Buhler et al. (2019), changed during the model run. Starting at the bottom, SMB varied based on orbital parameters. Mass is total mass accumulated over the region. Max Δh is max thickness among all points. Max T is maximum temperature, at the base of the thickest deposit. It is linearly influenced by thickness and dependent on thermal conductivity and geothermal flux that are fixed. Max V is maximum velocity. Velocity peaks at ~ 470 ka, during a period of positive SMB, at a location with the steepest slope.

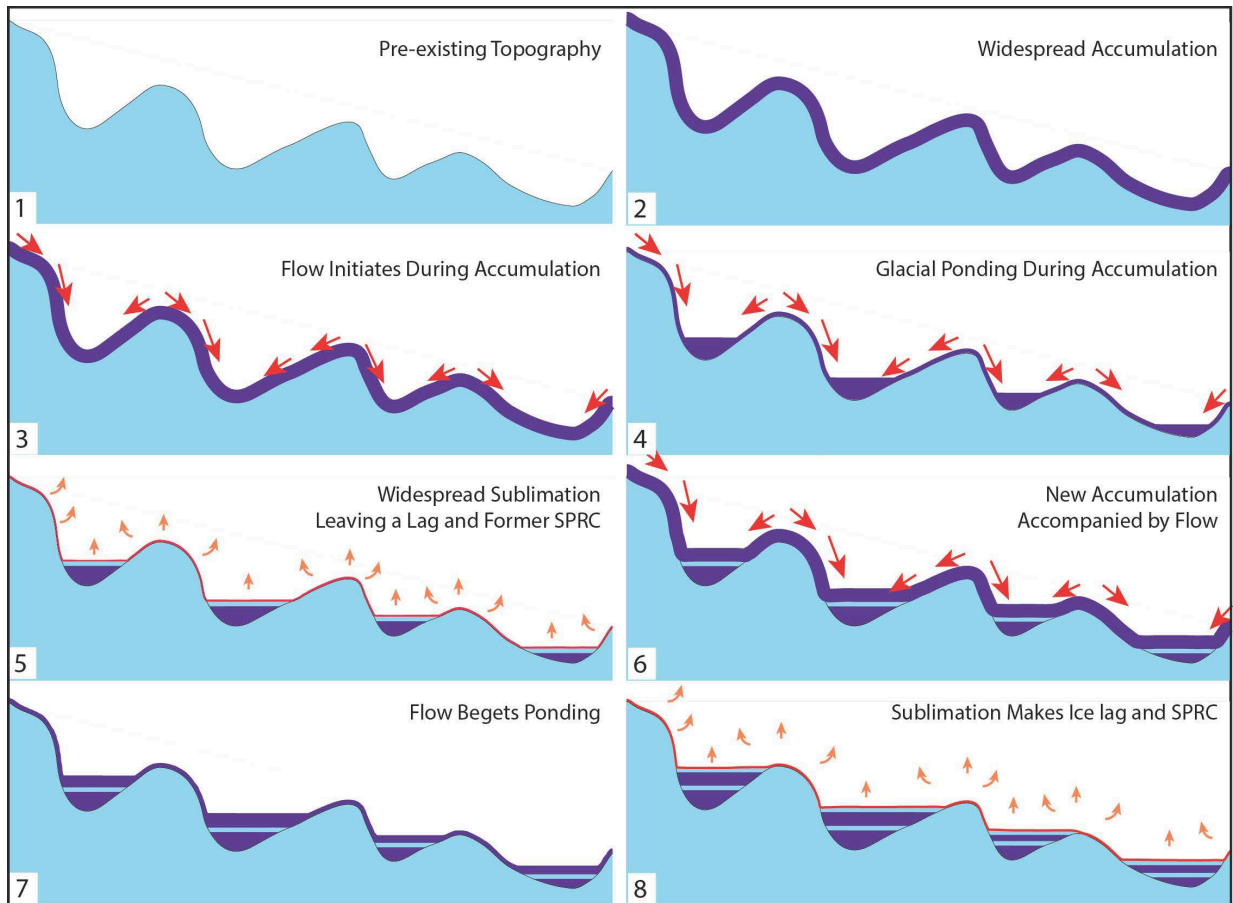


Figure 7: Heuristic model showing how flow affects the total thickness and final location of the massive CO₂ ice. 1) Pre-existing topography as observed by SHARAD (Putzig et al., 2018). 2) Uniform accumulation over the entire region (Buhler et al., 2019). 3 & 4) Flowing ice finds local topographic minima, where it ponds. 5) Sublimation over the entire region removes a thin unit of ice but leaves the thicker ponded ice, an H₂O ice lag/bounding layer, and a residual cap (red unit, per Buhler et al., 2019). 6 - 8) Repeat of steps 2-5, resulting in the current end member, with a surface lag and SPRC formation.

Supplemental Material for
Carbon Dioxide Ice Glaciers at the South Pole of Mars

I. B. Smith^{1,2}, N-J. Schlegel³, E. Larour³, I. Isola¹, P. Buhler², N. E. Putzig², R. Greve^{4,5}

¹York University, Toronto, Ontario, Canada M3J 1P3

²Planetary Science Institute, Lakewood, Colorado, 80401

³Jet Propulsion Laboratory, California Institute of Technology, Pasadena, California, 91109

⁴Institute of Low Temperature Science, Hokkaido University, Sapporo 060-0819, Japan

⁵Arctic Research Center, Hokkaido University, Sapporo 001-0021, Japan

Corresponding author: Isaac B Smith (ibsmith@yorku.ca)

Table of Contents

Supplemental Discussion, Images, and Methods	3
1 Geologic Interpretations	3
2 Modeling Methods	9
3 Modeling Results	10
4 Estimating topography, thickness, and base without data	13
References	14

1 Geologic Interpretation:

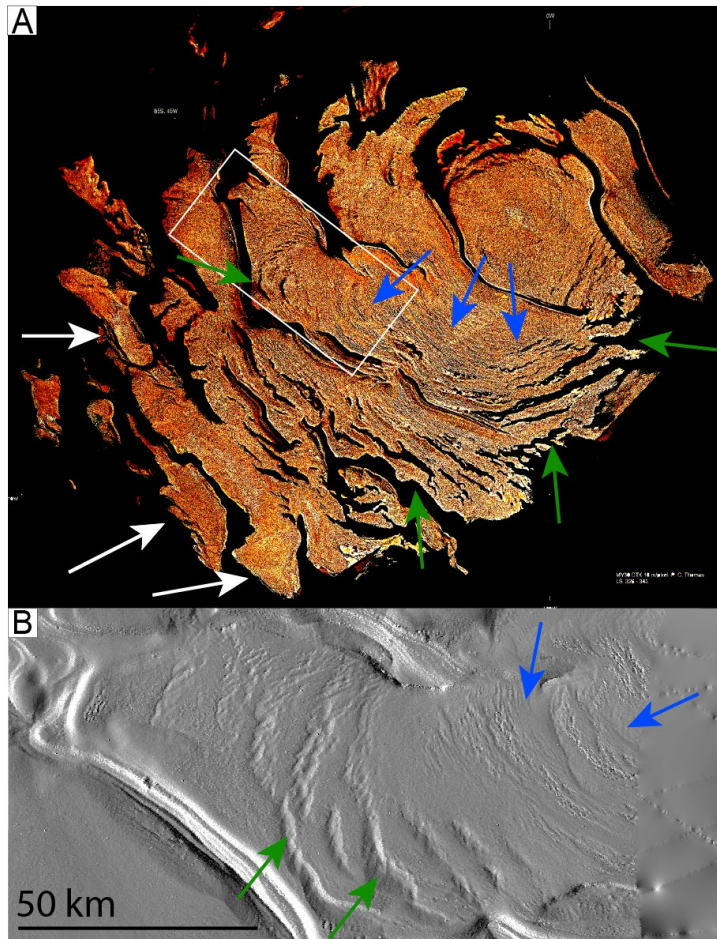


Figure S1: Minor troughs in imagery and topography. A) Mars Year 31 south polar CTX mosaic (Thomas et al., 2009) that has been high pass filtered and tinted orange to accentuate surface roughness caused by the minor troughs. Minor troughs are densest, smallest, and shallowest at the highest elevations and where the CO₂ ice is thickest (blue arrows). Minor troughs are largest and have the longest wavelengths near the greatest slopes of the CO₂ deposits, where we expect stresses to be greatest (green arrows). Deposits at lower elevations have few or no minor troughs (white arrows). B) MOLA Hillshade of region indicated in (A)

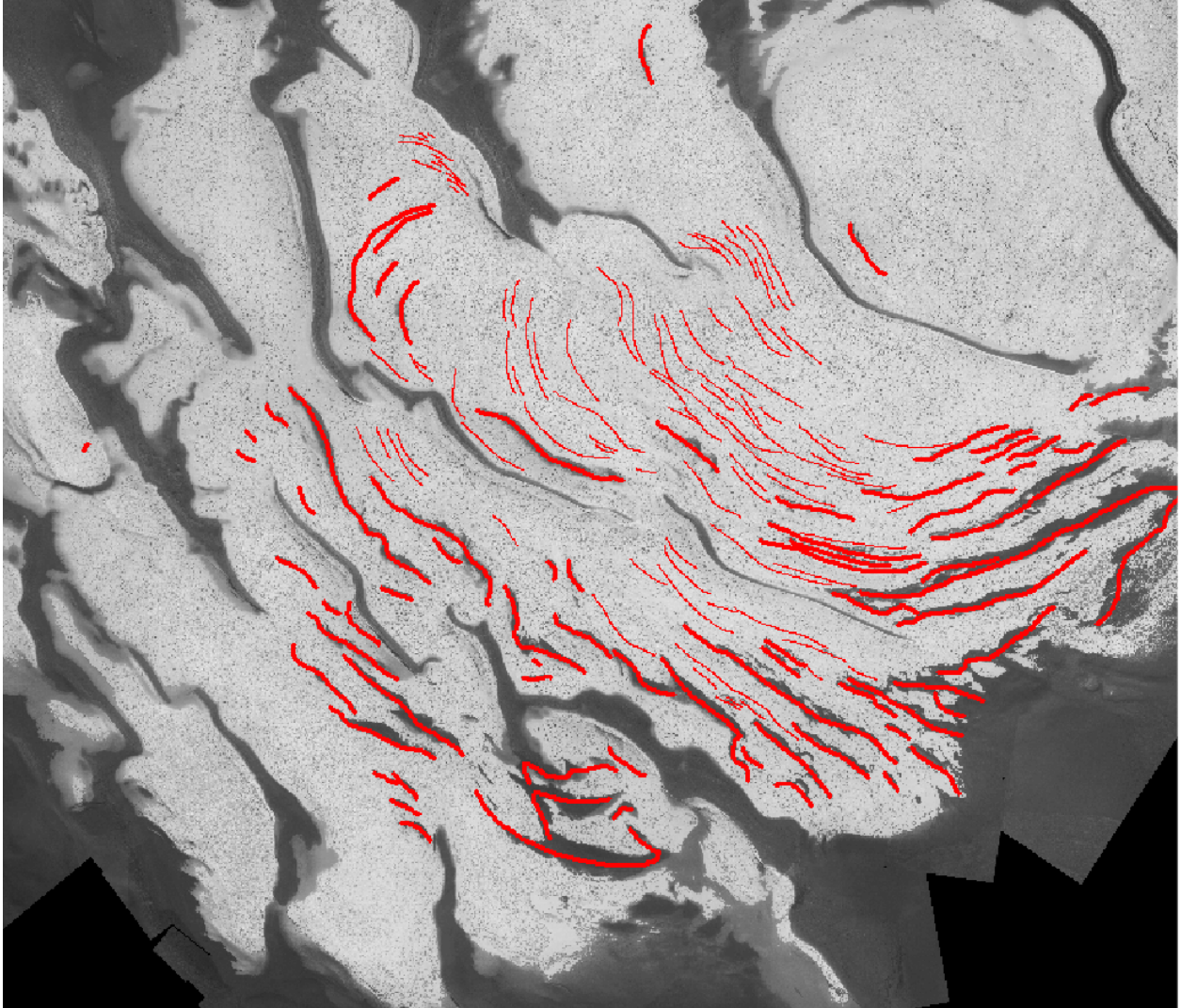


Figure S2: Mapped minor troughs that we interpret to be crevasses on top of a CTX mosaic (Thomas et al., 2009). The locations of these crevasses can be input into the ISSM model for treatment as rifts in the ice.

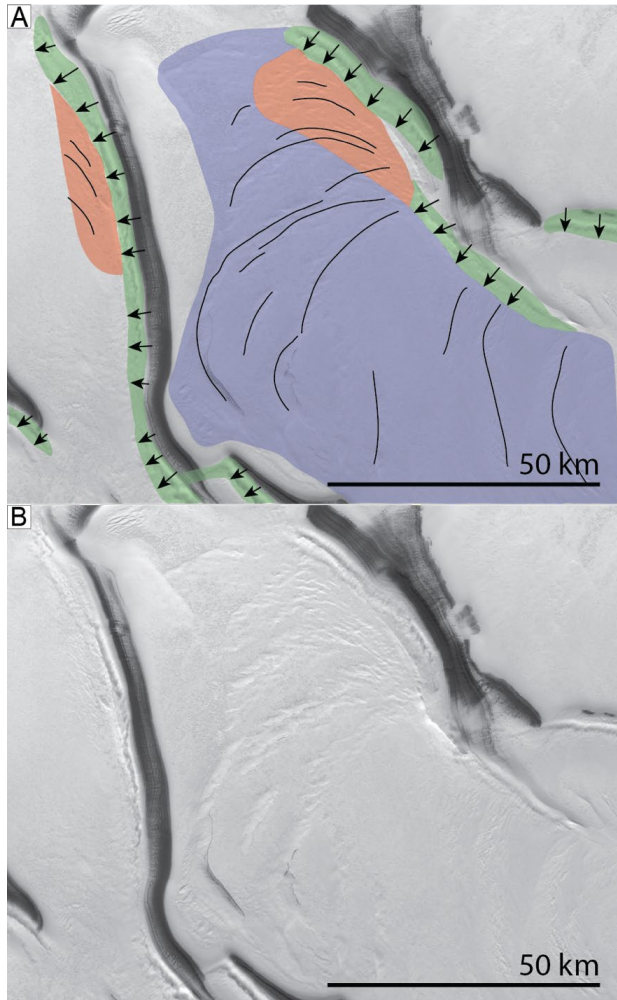


Figure S3: High Resolution Stereo Camera (HRSC) image showing the orientation of trough clouds and minor troughs. A) Annotated image showing regions with trough clouds (green), ridges (orange), and minor troughs (black lines). Wind directions (black arrows) inferred from cloud directions (Smith et al., 2013; 2014; Smith & Spiga, 2018) are not aligned with compression ridges or minor troughs (black lines). Blue field denotes locations with just minor troughs. Orange fields indicate locations with compression ridges (Figure 4) B) Unannotated HRSC image H2181_0000_ND3.

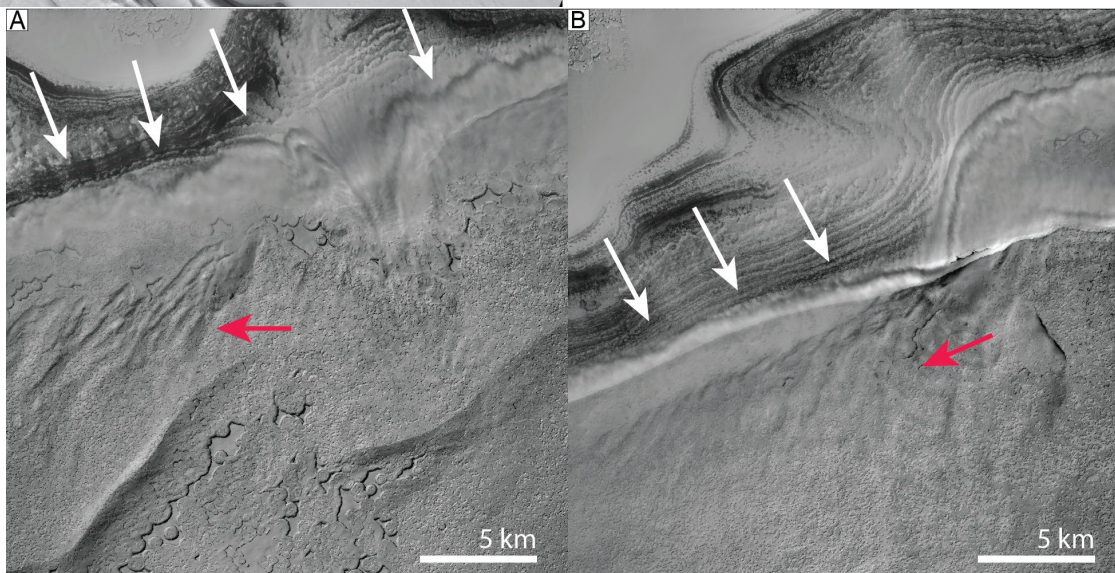


Figure S4: Ridges and trough clouds at the CO₂ margins. Trough clouds indicate that prevailing winds are towards the lower right (white arrows), but the ridges align neither perpendicular nor parallel to the inferred winds (indicated by red arrows). The ridges resemble compression ridges found at the margins of terrestrial ice flows (Figures 4 and S6)

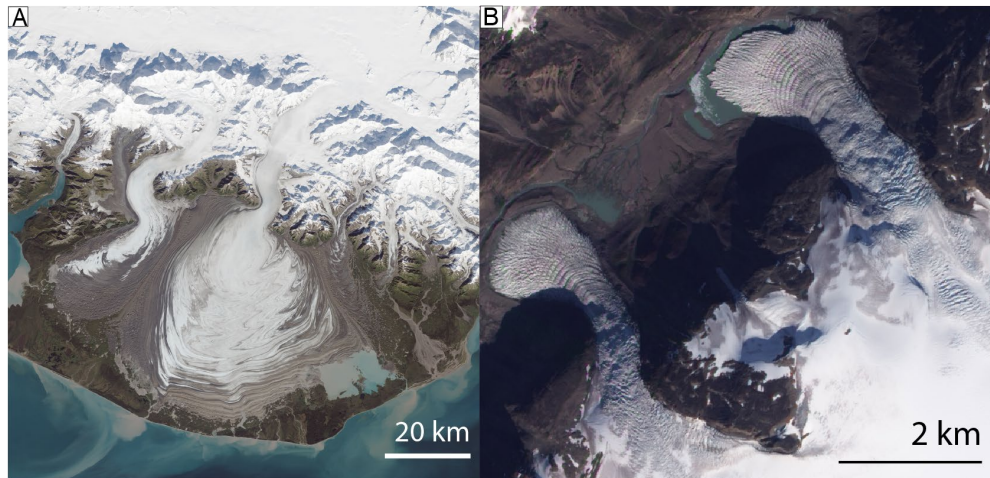


Figure S5: A) Landsat 8 - OLI image showing Malaspina glacier at $59^{\circ}55' N - 140^{\circ}32' W$ in Alaska taken on September 24, 2014. Arcuate landforms cover the surface. B) Arcuate depressions on outlet glaciers on the Sukkertoppen Ice cap in Greenland at $66^{\circ}07' N - 51^{\circ}31' W$. Photo taken on August 29, 2009 by the Advanced Land Imager ([ALI](#)) on NASA's Earth Observing-1 ([EO-1](#)) satellite. Crevasses in terrestrial glaciers exhibit the same arcuate landform as minor troughs seen on the south polar layered deposits SPLD (Figure 3).



Figure S6: Compression ridges adjacent to Ross Island, Antarctica. Top: Compression ridges between 3 and 5 m high, from the surface of the Ross Ice Shelf. Humans for scale. Bottom: Mosaic of photos taken from Observation Hill at different times. Fast ice flows from left towards slower moving ice and buckles, forming the ridges. Photo credits: I. B. Smith.

Crevasses:

Previous work by this team interpreted the minor troughs as being related to the prevalent winds (Smith et al., 2014); however, we rule out this hypothesis because the inferred and modeled wind directions are neither perpendicular nor parallel to the minor troughs, reducing the fidelity of a wind-transport mechanism. This would require an unlikely scenario in which winds transport material in a direction different than the wind vector.

To determine wind direction, we use trough clouds, a reliable indicator for inferring wind directions (Smith et al., 2013), and observe them to orient with wide variation in relation to the minor troughs and compression ridges (Figures S3, S4). Winds vectors, if they were to cause minor troughs as predicted in previous interpretations (Smith et al., 2014), should be perpendicular to the minor troughs (and the trough clouds parallel to the minor troughs) with little variability, making them unlikely to be the primary driver of minor trough orientation. For the low relief ridges, there is no obvious alignment with respect to wind orientations (Figures 4, S3, and S4), and we believe that preferential deposition or ablation (an alternative scenario to a construction based on wind transport) on these narrow features is unlikely.

Crevasse Formation

Stresses that break an uppermost water layer would expose the underlying CO₂ to atmospheric pressure and temperature, permitting more rapid sublimation (Figure S7) than through a vapor diffusion mechanism that makes the SPRC (Buhler et al., 2019). Fracture formation may even provide the dominant source of sublimating MCID during epochs in which flow is fast enough to create the stresses necessary for fracturing like at present.

During sublimation, crevasses that expose the lower ice would grow wider until some process produced a protective layer that would inhibit sublimation. At each location, we observe a layer of water ice covering the crevasses, consistent with the scenario in which they are no longer widening. Previous work has found no evidence of CO₂ ice in these minor troughs (Seelos et al., 2016).

Thus, due to sublimation and stresses, initially small curvilinear fractures could expand for long periods, widening and lengthening as the lower CO₂ ice continues to flow, to reach the dimensions we observe now at the lower sections of each elongated, curvilinear flow feature. The interpretation that the crevasses form by brittle deformation of water ice overriding less viscous carbon dioxide ice is supported by the fact that minor troughs are not present in the filled basins

(Figures S1 and S2), where driving stresses are much lower. The brittle water ice may withstand the reduced stress from low slopes and flow velocity.

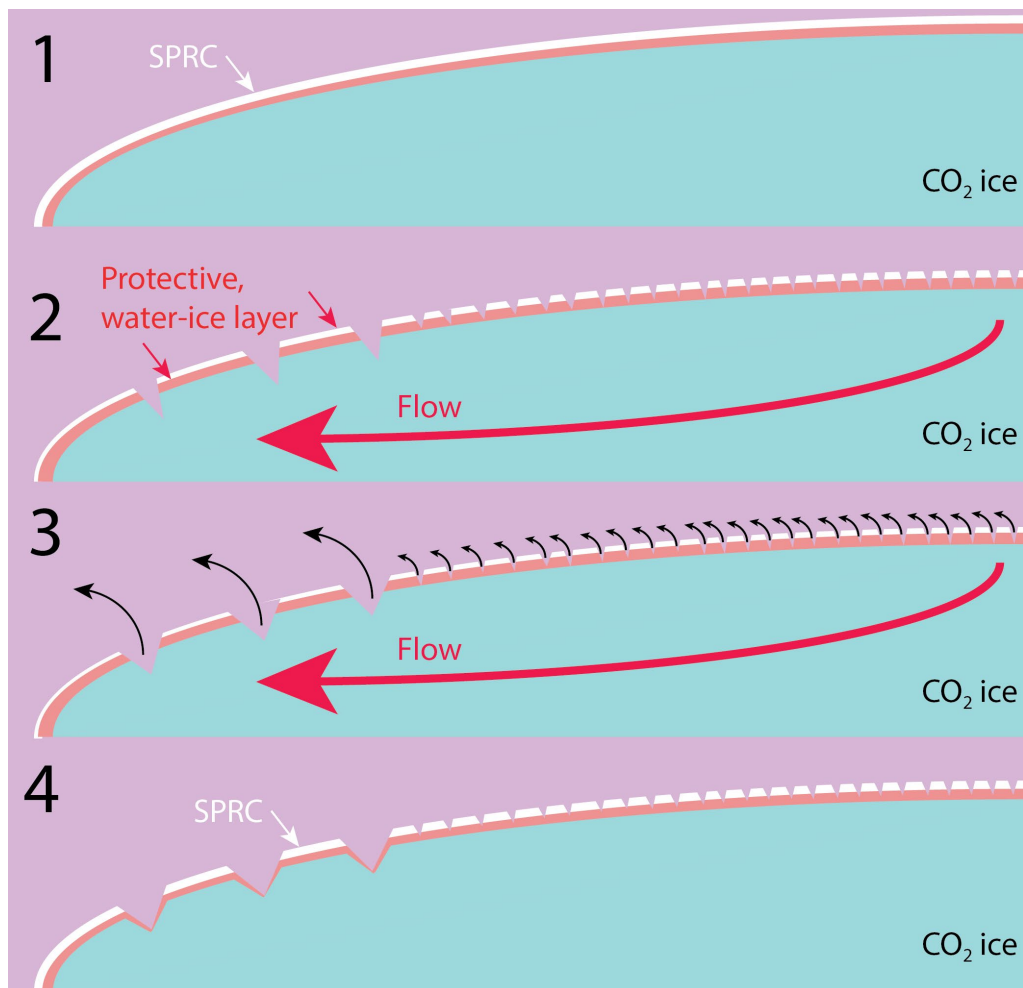


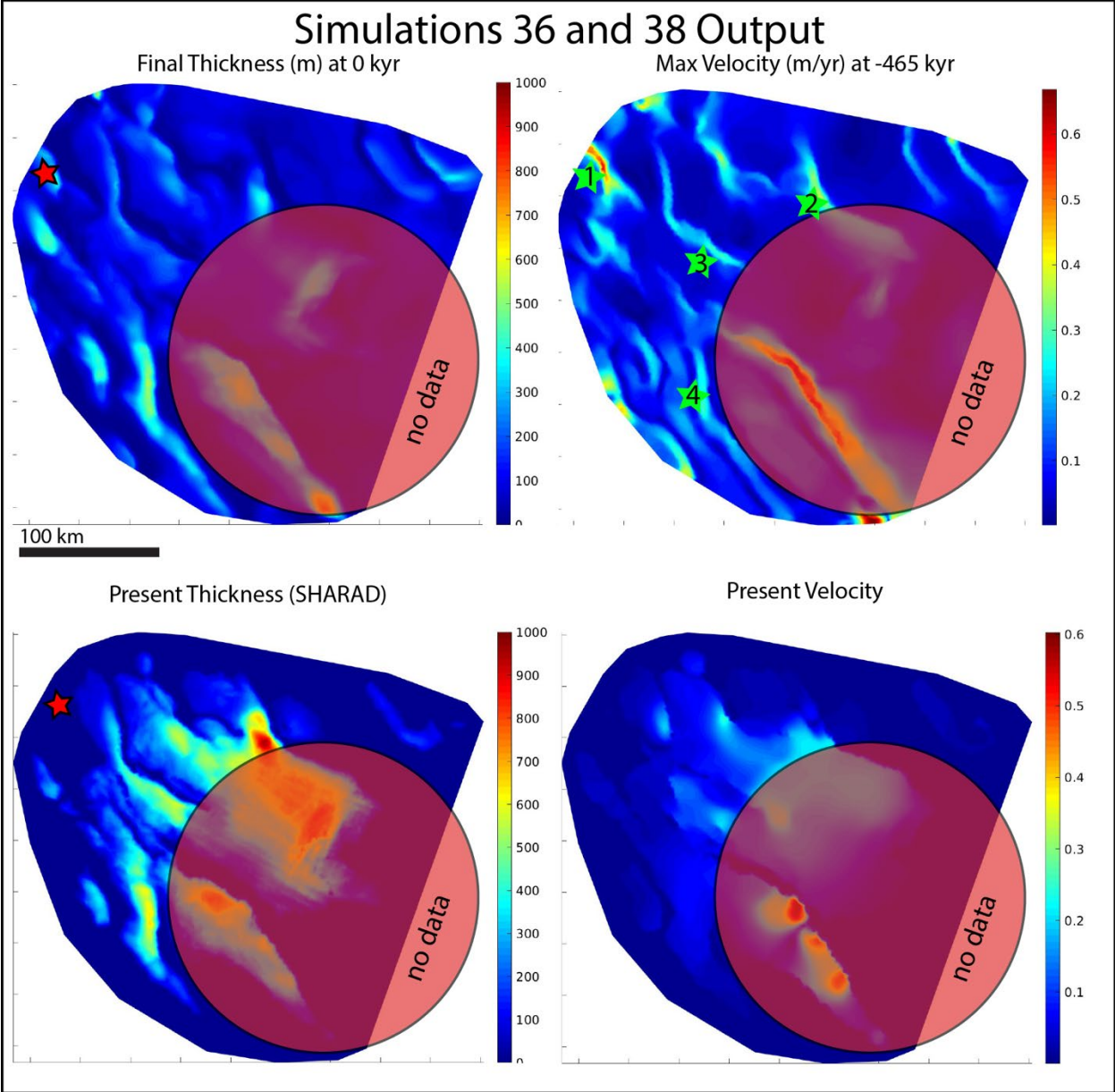
Figure S7: Crevasse formation scenario with flow and sublimation. 1) Brittle water ice capped with a residual cap of CO₂ locks the lower CO₂ in place. 2) When the SPRC sublimates, it exposes the lower albedo unit below; the entire body warms, and the CO₂ viscosity reduces. Then, the water ice cap fractures perpendicular to the driving stresses, rafting the water ice and permitting flow to occur. 3) Flowing CO₂ ice carries brittle water-ice above while sublimation (black arrows) widens the crevasses. 4) Sublimation of CO₂ leads to cold-trapping of water ice, filling the crevasses and strengthening the shell. The SPRC returns, and flow is further reduced because of the colder surface temperature. Blue is CO₂ ice; red is capping water-ice unit; white is SPRC.

2 Modeling Methods:

Sim #	Base and Topography	Start time/ Stop Time	geothermal flux	σ	Area m ² x10 ¹¹	Domain and Base
08-11	MOLA and SHARAD except inside of data gap, where this is originally interpolated by hand	600 ka to present	10 mW/m ²	n=8	1.4763	Domain 1 Base 1, Thick 1
12	Present-day setup	present to 1,000 yrs	10 mW/m ²	n=8	1.4763	Domain 1 Base 1, Thick 1
17-18	MOLA and SHARAD except inside of data gap, where this is newly interpolated by hand	510 ka to present	10 mW/m ²	n=8	1.7184	Domain 2, Base 2, Thick 2
19	Same as Sim 17-18	510 ka to present	10 mW/m ²	Flow Off	1.6620	Domain 3 Base 2, Thick 2
20-24	Same as Sim 17-18	510 ka to present	10 mW/m ²	n=8	1.6620	Domain 3 Base 2, Thick 2
25-26	Same as Sim 17-18	510 ka to present	10 mW/m ²	n=6	1.6620	Domain 3 Base 2, Thick 2
36	Included HRSC DTM for surface inside of MOLA hole	present to 1,000 yrs	25 mW/m ²	n=8	1.4763	Domain 1 Base 3, Thick 3
37	Same as Sim 36	510 ka to present	25 mW/m ²	n=8	1.4763	Domain 1 Base 3, Thick 3
38	Same as Sim 36	600 ka to present	25 mW/m ²	n=8	1.4763	Domain 1 Base 3, Thick 3

Table S1: Each simulation with relevant information and notes.

Because of the long periods to run each simulation on our workstation, many simulations suffered from a fault, such as a power outage or freezing, that required restarting. This is why simulation names have hyphens (e.g. 08-11, 17-18, 30-33).



3 Modeling Results

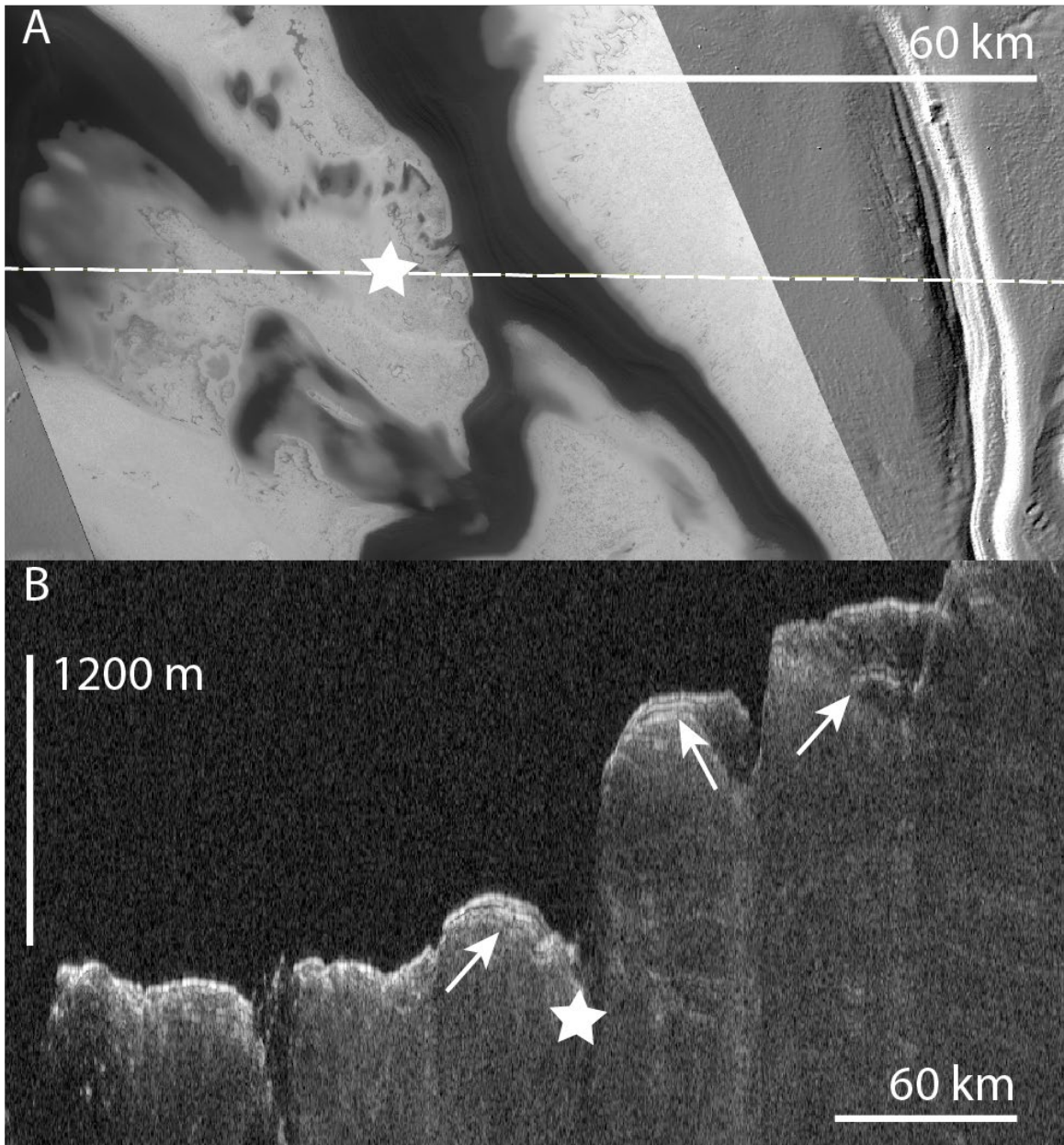


Figure S9: Search for evidence of former thick deposits at anomalous location. A): HRSC image HRSC_H2372_0000_ND3 showing the location where thick deposits are expected from modeling. Dashed line demonstrates the ground track of SHARAD observation in (B). B) SHARAD observation 2746001. Evidence for a thick deposit is lacking; however, layering (white arrows) indicates that H₂O deposition has occurred recently, perhaps as a result of the bounding layers remaining after sublimation depleted the MCID. Stars correspond to the same location.

4 Estimating topography, thickness, and base without data:

For our early simulations, we did not have access to the new HRSC high-latitude digital terrain model (Putrie et al., 2019). MOLA only provided data to 86.95° S, which left $>3^\circ$ of area without topographic information. Three-dimensional radar analysis improved upon this with because MRO has an orbit that reaches 87.45° (Putzig et al., 2018). A total of $>14,000$ km² were added to SPLD topographic data, but important data for calculating flow, namely basal slope and ice thickness, were still missing.

Running the ISSM simulations with interpolated data, where no geologic information is incorporated resulted in final CO₂ geometries that were implausible because of steep slopes towards 90° S. Because of that, we created estimates of surface and basal topography based on visual clues. For example, in locations with data that had minor troughs/crevasses, these features were perpendicular to the topographic gradient (Figures S1, S2). Thus, we assumed this trend would continue into the no-data zone and created a topography that reflected this assumption by making the surface slope away from the known topographic high and perpendicular to the crevasses. Additionally, two deposits of the MCID have similar expressions. One is on either side of the data discontinuity, and so, we used the measured unit to provide a similar topography to the one that was not measured, e.g. both are confined on three sides and had no crevasses, telling of a shallow slope away from the main unit but bound on the margins. Using these visual clues we created a topography and thickness. With the HRSC topography, we were able to eliminate one of the variables, and every simulation starting with 36 uses Putrie et al. (2019) results.

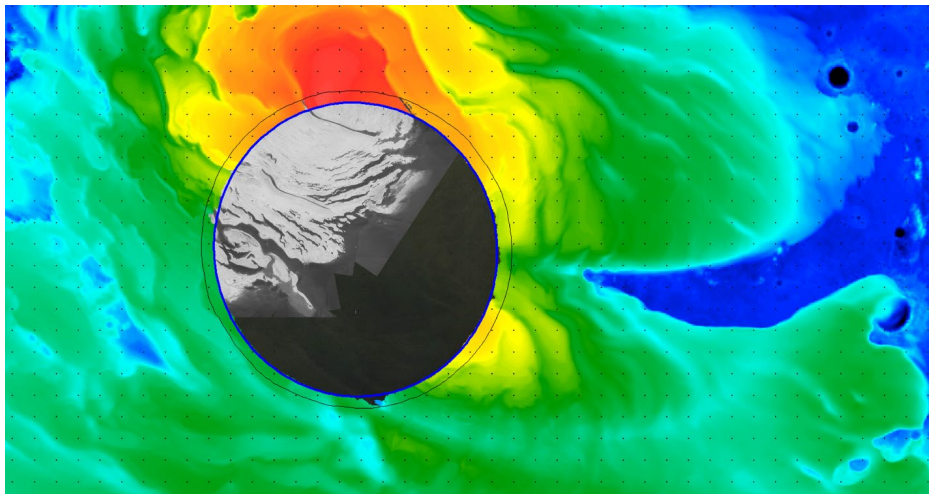


Figure S9: Mosaic of MOLA derived topography overlying a CTX mosaic to provide visual clues about the topography in the region with no data (inner circle).

References

- Buhler, P.B., Ingersoll, A.P., Piqueux, S., Ehlmann, B.L., Hayne, P.O., 2019. Coevolution of Mars's atmosphere and massive south polar CO₂ ice deposit. *Nat. Astron.* 1–8. <https://doi.org/10.1038/s41550-019-0976-8>
- Colaprete, A., Barnes, J.R., Haberle, R.M., Hollingsworth, J.L., Kieffer, H.H., Titus, T.N., 2005. Albedo of the south pole on Mars determined by topographic forcing of atmosphere dynamics. *Nature* 435, 184–188.
- Putri, A.R.D., Sidiropoulos, P., Muller, J.-P., Walter, S.H.G., Michael, G.G., 2019. A New South Polar Digital Terrain Model of Mars from the High-Resolution Stereo Camera (HRSC) onboard the ESA Mars Express. *Planet. Space Sci.* 174, 43–55. <https://doi.org/10.1016/j.pss.2019.02.010>
- Putzig, N.E., Smith, I.B., Perry, M.R., Foss, F.J., Campbell, B.A., Phillips, R.J., Seu, R., 2018. Three-dimensional radar imaging of structures and craters in the Martian polar caps. *Icarus, Mars Polar Science VI* 308, 138–147. <https://doi.org/10.1016/j.icarus.2017.09.023>
- Seelos, K.D., Brown, A.J., Calvin, W.M., Titus, T.N., Smith, I.B., Murchie, S.L., 2016. Exploring Mars' South Polar Residual Cap Units Using CRISM Data: Search for the Signature of Buried Ice Layers. Presented at the Lunar and Planetary Science Conference, p. 2130.
- Smith, I.B., Holt, J.W., Spiga, A., Howard, A.D., Parker, G., 2013. The spiral troughs of Mars as cyclic steps. *J. Geophys. Res. Planets.* <https://doi.org/10.1002/jgre.20142>
- Smith, I.B., Spiga, A., Holt, J.W., 2014. Aeolian processes as drivers of landform evolution at the South Pole of Mars. *Geomorphology, Planetary Geomorphology: Proceedings of the 45th Annual Binghamton Geomorphology Symposium, held 12-14 September 2014 in Knoxville, Tennessee, USA* 240, 54–69. <https://doi.org/10.1016/j.geomorph.2014.08.026>
- Smith, I.B., Spiga, A., Holt, J.W., 2015. Aeolian processes as drivers of landform evolution at the South Pole of Mars. *Geomorphology, Planetary Geomorphology: Proceedings of the 45th Annual Binghamton Geomorphology Symposium, held 12-14 September 2014 in Knoxville, Tennessee, USA* 240, 54–69. <https://doi.org/10.1016/j.geomorph.2014.08.026>